Complementing XCO_2 imagery with ground-based CO_2 and $^{14}CO_2$ measurements to monitor CO_2 emissions from fossil fuels on a regional to local scale

Elise Potier[1], Grégoire Broquet[1], Yilong Wang[1,2], Diego Santaren[1], Antoine Berchet[1], Isabelle Pison[1], Julia Marshall[3], Philippe Ciais[1], François-Marie Bréon[1], and Frédéric Chevallier[1]

[1]Laboratoire des Sciences du Climat et de l'Environnement, LSCE/IPSL, CEA-CNRS-UVSQ, Université Paris-Saclay, F-91191 Gif-sur-Yvette, France
[2]Key Laboratory of Land Surface Pattern and Simulation, Institute of Geographical Sciences and Natural Resources Research, Chinese Academy of Sciences, Beijing, China.
[3]Max Planck Institute for Biogeochemistry (MPI-BGC), Jena, Germany. Now at Deutsches Zentrum für Luft- und Raumfahrt (DLR), Institut für Physik der Atmosphäre, Oberpfaffenhofen, Germany

Correspondence: Elise Potier (elise.potier@lsce.ipsl.fr)

Abstract. Various satellite imagers of the vertically integrated column of carbon dioxide (XCO_2) are under development to enhance the capabilities for the monitoring of the fossil fuel (FF) CO_2 emissions. XCO_2 images can be used to detect plumes from cities and large industrial plants, and to quantify the corresponding emissions using atmospheric inversions techniques. However, this potential and the ability to catch the signal from more diffuse FF CO_2 sources can be hampered by the mix

5   between these FF signals and a background signal from other types of CO_2 surface fluxes, and in particular of biogenic CO_2 fluxes. The deployment of dense ground-based air-sampling networks for CO_2 and radiocarbon ($^{14}CO_2$) could complement the spaceborne imagery by supporting the separation between the fossil fuel and biogenic or biofuel (BF) CO_2 signals. We evaluate this potential complementarity with a high resolution analytical inversion system focused on Northern France, Western Germany, Belgium, Luxembourg and a part of the Netherlands, and with pseudo-data experiments. The inversion system

10   controls the FF and BF emissions from the large urban areas and plants, in addition to regional budgets of more diffuse emissions or of biogenic fluxes (NEE, Net Ecosystem Exchange), at an hourly scale over a whole day. The system assimilates pseudo data from a single track of a 300-km swath XCO_2 imager at 2 km resolution and from surface ground-based CO_2 and/or $^{14}CO_2$ networks. It represents the diversity of $^{14}CO_2$ sources and sinks and not just the dilution of radiocarbon-free FF CO_2 emissions. The uncertainty in the resulting FF CO_2 emissions at local (urban area/ plant) to regional scales is directly derived

15   and used to assess the potential of the different combinations of observation systems. The assimilation of satellite observations yield estimates of the morning regional emissions with an uncertainty down to 10% (1 sigma) in the satellite field of view, from an assumed uncertainty of 15% in the prior estimates. However, it does not provide direct information about emissions outside the satellite field of view and neither about afternoon or nighttime emissions. The co-assimilation of $^{14}CO_2$ and CO_2 data lead to a further reduction of the uncertainty in the estimates of FF emissions. However, this further reduction is significant

20   only in administrative regions with three or more $^{14}CO_2$ and CO_2 sampling sites. The uncertainty in the estimates of 1-day emission in North Rhine-Westphalia, a region with three sampling sites, decreases from 8 to 6.6% when assimilating the in

situ $^{14}CO_2$ and CO_2 data in addition to the satellite data. Furthermore, this new decrease appears to be larger when the ground stations are close to large FF emission areas, providing an additional direct constraint for the estimate of these sources rather than supporting the characterization of the background signal from the NEE and its separation from that of the FF emissions.

1 Introduction

Article 4 of the Paris Climate Agreement aims to reduce greenhouse gas (GHG) emissions within a few decades on the basis of equity, until they are compensated by GHG removals. The monitoring of this international ambition implies some operational observation of the GHG emissions, in particular those of carbon dioxide (CO_2) from fossil fuels (FFs). A significant contribution to this monitoring is expected from observations of atmospheric composition and atmospheric inversion systems (IPCC, 2019; Ciais et al., 2015; Pinty et al., 2017). In particular, the development of spaceborne imagery of the vertically integrated column of CO_2 (XCO_2), at spatial resolution better than 5 km, should make it possible to detect plumes under the wind from anthropogenic sources of CO_2 (Pillai et al., 2016; Schwandner et al., 2017; Broquet et al., 2018). A key example of such imagery is the Copernicus Anthropogenic Carbon Dioxide Monitoring (CO2M; Pinty et al., 2017) constellation which is schedule to launch in 2025-2026. Each satellite of the constellation will observe XCO_2 with a $\sim 300\,km$ swath and a $\sim 2 \times 2\,km^2$ spatial resolution.

Previous analyses of the potential of high resolution satellite imagery (such as ESA, 2015; Broquet et al., 2018; Santaren et al., 2021; Wang et al., 2020; Kuhlmann et al., 2019) have focused on its use as a stand-alone observation system. However, the distinction between FF and natural CO_2 signals and thus the separation between the FF and natural components in the flux estimates remain difficult, even when using high-resolution images (Santaren et al., 2021). The separation between the emissions from biofuel (BF) and FF combustion is another challenge because BF emissions can be located in the same hot-spots as FF ones (Ciais et al., 2020).

The deployment of dense ground-based networks of near-surface air sampling for radiocarbon ($^{14}CO_2$) has been considered in complement to the spaceborne imagery (Ciais et al., 2015). Indeed FF-emitted CO_2 is radiocarbon-free (Pinty et al., 2017; Wang et al., 2018; Levin et al., 2003; Wang, 2016; Basu et al., 2016): $^{14}CO_2$ surface data have a less ambiguous sensitivity to the signal from FF emissions than CO_2 surface data. However, practical constraints lead to sampling $^{14}CO_2$ daily if not weekly to monthly. This prevents the direct identification of temporal variations at higher frequencies, e.g. hourly, associated with the signal from cities and point sources, but time series of continuous hourly measurements of CO_2 should enable these specific temporal variations to be captures.

This study aims at assessing the potential of combination between a spaceborne XCO_2 imager and ground based $^{14}CO_2$ and CO_2 networks to monitor FF emissions of CO_2. More specifically, it aims at assessing how these additional ground-based networks decrease the uncertainty in FF emissions by improving the distinction between the FF and biogenic fluxes. The inversion tests performed in this study with different sets of pseudo-data correspond to Observing System Simulation Experiments (OSSEs). They include the simulation of the sampling of a CO2M-like spaceborne instrument from single orbits over Western Europe at 12:00 (Universal Time Coordinated, UTC).

55 The work performed relies on a Bayesian inversion framework, in which the knowledge of control parameters, here the CO_2 fluxes, improves with the assimilation of related observations. It is focused on the direct computation of the uncertainty in the control parameters. We analyse the uncertainty in the *posterior* values of the control parameters as a function of the observation system that is used for the inversion, and the corresponding uncertainty reduction, i.e., the relative difference between the posterior uncertainty and the prior uncertainty in the control parameters.

60 The analysis of this uncertainty reduction is made at the local scale (urban areas, industrial plants) to the regional scale, following the rationale and the general inverse modelling framework of Santaren et al. (2021). It focuses on a large part of Western Europe, using a configuration of the CHIMERE regional transport model (Menut et al., 2013) with a 2 km horizontal zoom over Northern France, Western Germany, Belgium, Luxembourg and a large part of the Netherlands. It controls FF emissions from urban areas and industrial plants in addition to regional budgets of more diffuse emissions or of biogenic fluxes
65 at an hourly scale. The analytical expression of the inversion framework (Wu et al., 2016) allows for the results of the individual control parameters or for budgets integrated in space within the regions or in time within a day to be analyzed and for many options for the observation system to be tested despite the dimension of the high resolution inversion problem.

The assimilation of $^{14}CO_2$ and CO_2 surface data in addition to XCO_2 images and the inclusion of non-FF fluxes of $^{14}CO_2$ in the inversion framework make use of the larger-scale inversion framework developed by Wang (2016). It takes into account
70 not only the $^{14}CO_2$ emissions from nuclear power plants and fuel reprocessing plants, but also the specific isotopic signatures of the heterotrophic respiration (HR) and Net Primary Production (NPP) by land ecosystems and thus solves for these fluxes separately. It also controls the emissions from BF burning.

The analytical inversion framework is described in section 2. Results from the pseudo-data experiments with the assimilation of satellite observations alone are taken as a reference and presented in Section 3.1. Then a larger suite of experiments
75 combining $^{14}CO_2$ and CO_2 surface and XCO_2 satellite observations is used to assess their complementarity in Sections 3.2 to 3.3. Section 4 provides some discussions about this inversion framework and a conclusion regarding complementarity of XCO_2 satellite, $^{14}CO_2$ and CO_2 surface observations.

2 Methodology of the inversion

This section presents the high dimensional inversion framework designed in this study for the co-assimilation of CO_2 and
80 $^{14}CO_2$ data. It has strong similarities with the system developed by Santaren et al. (2021), which assimilates CO_2 data only, and it borrows from Wang (2016) to assimilate $^{14}CO_2$ data. The system relies on:

- An analytical inversion framework as presented in Section 2.1 in which budgets of surface anthropogenic and natural fluxes are controlled at local (city or industrial plant) or regional scales and at hourly resolution (see the definition of the control vector in Section 2.4).

85 - A zoomed configuration of the regional atmospheric transport model CHIMERE for most of Western Europe, described in section 2.2.

- Hourly to annual maps of all types of surface CO_2 and $^{14}CO_2$ fluxes, at high spatial resolution from the CO_2 Human Emissions project (CHE, https://www.che-project.eu/), which are described in section 2.3, at temporal resolutions up to 1-hour. They are used to distribute the local-to-regional-scale budgets of the fluxes into corresponding high resolution flux maps (see section 2.4).

- Simulations of the location, time and uncertainty of the XCO_2 retrievals and of the CO_2 and $^{14}CO_2$ ground-based data, for different scenarios of the observing system, as described in Section 2.5. For the XCO_2 data, we rely on the simulation of the CO2M sampling during one satellite pass over the area of interest generated by the Institut für Umweltphysik (IUPB) in the frame of the ESA-PMIF project (European Spacial Agency, Plume Monitoring Inversion Framework Wang et al., 2020; Lespinas et al., 2020).

Inversions are conducted over a 1-day window from 0:00 to 24:00, on July 1 2015, i.e. in summer when the biogenic fluxes are relatively high. The restriction to 1 day is connected to results of Santaren et al. (2021), which show the lack of sensitivity of observations made during a given day to the fluxes during other days over the modeling domain, and to the large computation cost associated with the preparation of a full day of analytical inversion. With such an inversion window, wider than the one chosen in Broquet et al. (2018) or Santaren et al. (2021), the system tracks the signal from the FF emissions up to 12 hours before the satellite overpass (see Section 2.5.1) and 10 hours before the in-situ data assimilation window (see Section 2.5.2). After a few hours, the air masses having been transported over typically 100 km, the signal from individual FF CO_2 sources (industrial plants, cities, regions) is much diffused and hardly detectable in XCO_2 images. Consequently this 1-day timescale is large enough to represent the full extent of the CO_2 FF plumes that can be exploited in images from CO2M-like instruments to compute the corresponding emissions (Broquet et al., 2018; Santaren et al., 2021). The ability to track large-scale budgets of FF emissions over longer time periods relies on complementary observations of FF emission tracers. These tracers, such as the $^{14}CO_2$ measurements considered here, may help filter a relatively low FF signal from the biogenic signal which is generally much larger over long distances (Pinty et al., 2017; Fortems-Cheiney et al., 2021). CO_2 and $^{14}CO_2$ ground-based networks could also reinforce the constraint on the FF CO_2 emission estimates during the few hours before the satellite overpass. By starting the inversion window 12 hours before the satellite overpass and 10 hours before the first surface measurement, we account for the full window of FF CO_2 emission, the estimate of which can potentially be directly constrained by these different datasets or by their combination.

2.1 Inversion general equation

Under the assumption that all uncertainties in the inversion problem have a Gaussian and unbiased distribution, these uncertainties are fully characterized by their covariance matrices. The analytical Bayesian inversion allows for the computation of the covariance matrix of the posterior uncertainty (uncertainty in the posterior estimate of the fluxes) $\mathbf{A}$ as a function of the observation operator $\mathbf{H}$ connecting the control parameters (the flux budgets, see section 2.4) to the observation vector (the space defined by the ensemble of pseudo observations, see section 2.5), of the covariance matrix of the prior uncertainties (uncertainty in the prior estimate of the fluxes, see section 2.4.2) $\mathbf{B}$ and of the model and observation errors covariance matrix

120   **R** (in the observation space, see section 2.5.3), following Tarantola (2005):

$$\mathbf{A} = [\mathbf{B}^{-1} + \mathbf{H}^T \mathbf{R}^{-1} \mathbf{H}]^{-1} \tag{1}$$

The observation operator **H**, is assumed to be linear and is decomposed, following the notations of Staufer et al. (2016), into :

$$\mathbf{H} = \mathbf{H}_{sample} \mathbf{H}_{transp} \mathbf{H}_{distr} \tag{2}$$

$\mathbf{H}_{distr}$ defines (i) the spatial and temporal distribution of the fluxes within each area corresponding to a control parameter

125   and beyond the temporal resolution of these control parameters, (ii) the flux budgets to be rescaled by the inversion for these areas at the control resolution, and (iii) the application of the isotopic signatures to CO_2 fluxes. Here, it is based on the flux products and on the signatures described in Section 2.3.

$\mathbf{H}_{transp}$ is the atmospheric transport operator, corresponding to our configuration of the transport model CHIMERE described in section 2.2.

130    $\mathbf{H}_{sample}$ corresponds to the computation of XCO_2 and to the sampling of XCO_2 or of near ground concentrations of CO_2 and $^{14}CO_2$ at the observation time and locations from the output of the CHIMERE model. Section 2.5 provides more details on this operator. The derivation of the **H** matrix in the analytical system requires an extensive set of simulations with the computation of the imprint (columns of **H**) of each of the control parameters (Santaren et al., 2021).

2.2   Atmospheric transport

135   ### 2.2.1   Transport model configuration

The transport operator of CO_2 and $^{14}CO_2$ in the atmosphere, $\mathbf{H}_{transp}$, relies on the CHIMERE transport model, driven here by the Community Inversion Framework (CIF, Berchet et al., 2021). The domain and the horizontal grid for the CHIMERE configuration used here are represented in Figure 1. They cover a part of Western Europe (longitude: -6.82° to 19.18°; latitude: 42.0° to 56.39°). The resolution of the horizontal grid varies between 50 and 2 km. The 2 km×2 km-resolution zoom covers

140   Northern France, Luxemburg, Belgium, a large part of the Netherlands and Western Germany (longitude: -1.25° to 10.64°; latitude: 47.45° to 53.15°). The vertical grid is composed of 29 pressure layers extending from 997 hPa to 300 hPa (from the surface to approximately 9 km above the ground level).

Our configuration of CHIMERE ignores chemistry since CO_2 and $^{14}CO_2$ are inert species at the time scale considered in this study (24 h). This explains why the resulting atmospheric transport operator $\mathbf{H}_{transp}$ is assumed to be linear. It is forced

145   by meteorological variables provided by the European Centre for Medium-Range Weather Forecasts (ECMWF) for the CHE project at 9 km resolution (Agusti-Panareda, 2018). Figure 2 provides indications on the typical horizontal transport conditions during the day of inversions over the area of interest: on July 1st 2015, a South-East wind over the North East part of the domain spreads the atmospheric signature of FF emissions in the North-West direction.
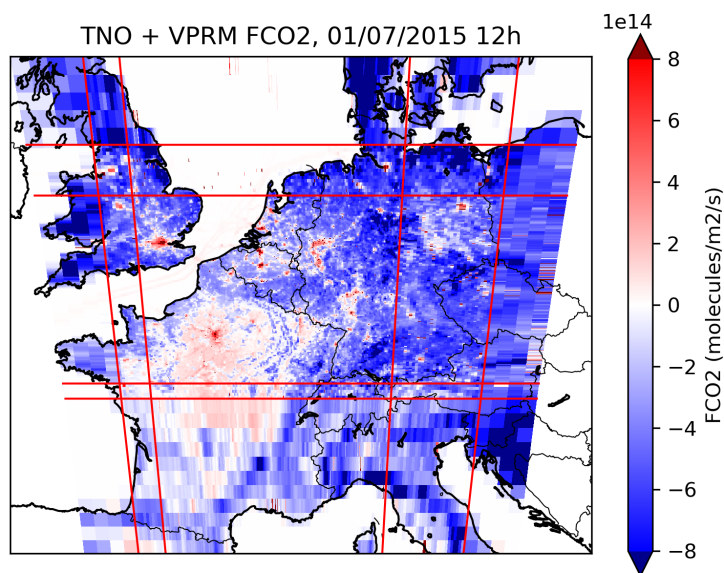
Figure 1. CO_2 flux map (based on values from the TNO inventory and VPRM simulations for 1 July 2015 at 12:00) over the atmospheric transport modelling grid. The red lines delimit the spatial resolution changes within the domain (from 2 km to 10 km and then 50 km from the middle to the edges of the domain)

2.2.2 Simulation of CO_2 and $^{14}CO_2$ transport

150   In this section, we present a formal decomposition of the CO_2 and $^{14}CO_2$ transport in order to introduce the notation and assumptions used in the inversion framework. The decomposition of the $^{14}CO_2$ transport and its formulation in a specific unit (parts per million per mil, ppm ‰) follow that of Wang (2016).

$$
\begin{aligned}
C_{a,CO2} = \mathbf{H}_{transp} \big[& F_{FF,CO2} + F_{BF,CO2} + \\
& F_{NPP,CO2} + F_{HR,CO2} \big] + \\
& H_{bc} \big[C_{bc,CO2} \big]
\end{aligned}
\tag{3}
$$

$$
\begin{aligned}
C_{a,CO2} \cdot \delta_a = \mathbf{H}_{transp} \big[& \delta_{FF} \cdot F_{FF,CO2} + \delta_{BF} \cdot F_{BF,CO2} + \\
& \delta_{NPP} \cdot F_{NPP,CO2} + \delta_{HR} \cdot F_{HR,CO2} + \\
& 1/R_{std} \cdot F_{Nucl}^{14C} \big] + \\
& H_{bc} \big[C_{bc,14CO2} \cdot \delta_{bc} \big]
\end{aligned}
\tag{4}
$$

(a) Morning
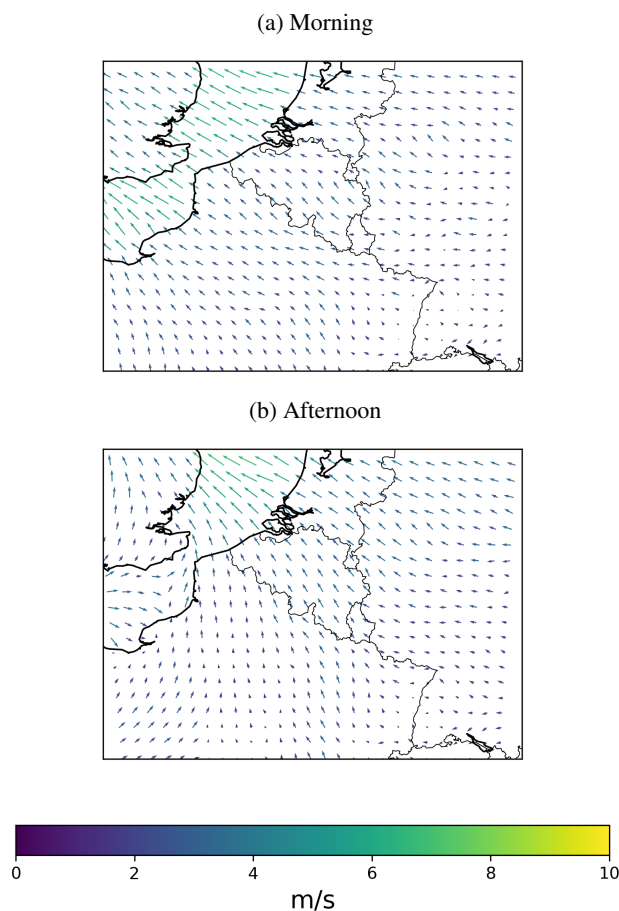
(b) Afternoon

Figure 2. Morning (a) and afternoon (b) wind averaged in the first two vertical layers of the CHIMERE grid (i.e., heights between 0 and 28 m above the ground)

155   where:

- $C_{a,CO2}$ is the CO_2 atmospheric concentration.

- F_x terms correspond to different types x of CO_2 fluxes within the transport modelling domain: FF emissions, BF emissions, NPP and HR.

- $C_{bc,x}$ are the boundary (top and lateral) and initial conditions of CO_2 and $^{14}CO_2$ concentrations, and $\mathbf{H}_{bc}$ their transport

160   within the modeling domain, but they are ignored in this inversion study (see Section 2.3.3).

- δ_a are the $^{14}CO_2/^{12}CO_2$ ratios in the atmosphere (R), normalized by the $^{14}C/^{12}C$ ratio in the Modern Standard ($(R/R_{std} - 1); R_{std} = 1.176 \times 10^{-12}$). Similarly, in the following, all δ are also normalized ratios.

- δ_x isotopic signature of the $^{14}CO_2$ fluxes listed above.

- F_{Nucl}^{14} corresponds to $^{14}CO_2$ fluxes from nuclear power plants.

2.3 Flux maps

2.3.1 CO$_2$ flux maps

The anthropogenic CO_2 emissions, from both FF and BF combustion, are derived from two inventories of the annual emissions produced by Netherlands Organisation for Applied Scientific Research (TNO) over Europe for the year 2015 (Denier van der Gon et al., 2017; Super et al., 2020). The emissions in the 2-km-resolution area of the domain are interpolated from a ~1 km (1/60°× 1/120°) resolution inventory (TNO_GHGco_1x1km_v1_1) which entirely covers this area but not the whole CHIMERE domain (its extent being -2°to 19°in longitude and 47°to 56°in latitude). The emissions in the rest of the CHIMERE domain are interpolated from a ~ 6 km (1/10°× 1/20°) resolution inventory (TNO_GHGco_v1_1, covering -30°to 60°, in longitude and 30°to 72°in latitude). These data are projected on the CHIMERE horizontal grid ensuring mass-conservation. The temporal disaggregation at hourly scale is based on coefficients depending on the sector of activity and the time zone provided in the CHE project (Marshall et al., 2019). Emissions from point sources are projected on the CHIMERE vertical grid depending on activity sectors while emissions from diffused sectors of activity (traffic, heating etc.) are emitted from the ground in the model.

No distinctions between CO_2 BF emissions from woods and crops is done in the TNO inventories. However this split is needed to derive $^{14}CO_2$ fluxes (see below). Consequently, assumptions are made based on emission categories used in TNO inventory, i.e. the Gridded Nomenclature For Reporting (GNFR) of the United Nations Framework Convention on Climate Change (UNFCCC). In this study, we consider that BF from woods is burned in power plants and in the industry and residential sectors only, i.e. in categories A to C. BF from crops is burned in categories F and L only, that correspond to road transport and agriculture. We assume that the BF emissions from the other sectors are negligible since they represent less than 2 % of the total BF emissions in the vast majority of countries.

The CO_2 biogenic fluxes are interpolated from simulations at 1 h and 5 km resolution with the VPRM model (Vegetation Photosynthesis and Respiration Model, Mahadevan et al., 2008) for the year 2015, provided by MPI-Jena over Europe (over latitude 31°to 68.7°; longitude -35.5°to 60.5°). The VPRM simulations provide estimates of gross primary production (GPP) and total respiration. Daily partition coefficients (α_{HR}) are derived from ORCHIDEE-MICT simulations at 0.5°resolution over Europe in 2015 (Guimberteau et al., 2018) to scale GPP and Respiration from VPRM into NPP and HR fluxes. The total biogenic fluxes correspond to the Net Ecosystem Exchange (NEE = NPP + HR = GPP + Resp).

The total CO_2 fluxes for 1st July 2015 at 12:00 are presented in Figure 1.

2.3.2 Isotopic signatures and $^{14}CO_2$ flux maps

To produce $^{14}CO_2$ fluxes, corresponding isotopic signatures are applied to the CO_2 fluxes.

$\delta_{FF} = -1000‰$ was applied to F_{FF} on the whole year and domain.

We distinguish $\delta_{BF,wood}$ from $\delta_{BF,crop}$ because crops and wood have a different age at harvest resulting in different ^{14}C abundance. In a first approximation, we determined these δ_{BF} as a spatial and temporal average of $^{14}CO_2$ contains in vege-
200 tation, $\delta_{biomass}$, simulated with the emulator of the ORCHIDEE-MICT model (Guimberteau et al., 2018; Naipal et al., 2018; Wang, 2016) over the whole ORCHIDEE-MICT Europe domain in 2015, selecting the relevant plant functional types (PFT): non-tropical trees for $\delta_{BF,wood}$ or crops for $\delta_{BF,crop}$. Such a computation of δ_{BF} relies on the hypothesis that the wood or cropfuel burnt in Europe comes from European (López et al., 2017) and recently cut vegetation. As a result, $\delta_{BF,wood} = 95‰$ and $\delta_{BF,crop} = 19‰$.

205

δ_{NPP} monthly maps at 5 km spatial resolution were derived for application to the VPRM biogenic fluxes:

$$\delta_{NPP} = \delta_{a,surf} - \epsilon \tag{5}$$

where $\delta_{a,surf}$ is the radiocarbon signature in the surface atmospheric layer and ϵ is the sum of kinetic and enzymatic $^{14}CO_2$ fractionation with respect to $^{12}CO_2$ depending on the C3 or C4 photosynthesis pathway of the vegetation.
210 $\delta_{a,surf}$ is characterized by a conversion of Δ14C monthly background measurements at Schauinsland in Germany, in 2015 (Hammer and Levin, 2017) following Stuiver and Polach (1977) with δ_{13C} from Graven et al. (2017). This ratio varies between 46 and 49 ‰. Here, we neglect the impact of variations of this $\delta_{a,surf}$ at high spatial and temporal resolution on the $^{14}CO_2$ NPP fluxes themselves. Accounting for such variations for a precise computation of the δ_{NPP}, and so $^{14}CO_2$ NPP fluxes, would have required a dynamical computation with $\delta_{a,surf}$ depending on $^{14}CO_2$ concentrations calculated by the transport
215 model and would have introduced strong non-linearities in the inversion (with an evolving **H**). However, over one day, these variabilities are assumed to be negligible as was found by Wang (2016) within each region-month.

The value of ϵ is 36 ‰ for C3 vegetation and 8 ‰ for C4 vegetation as described by Wang (2016) from Farquhar et al. (1989) and Degens (1969). We derive the C3/C4 distribution on the VPRM grid and per month, from the combination of three land cover maps: the VPRM and ORCHIDEE land cover maps and monthly MIRCA2000 crop map (Portmann et al., 2010). This
220 combination allows us to capitalise on the high spatial resolution of the VPRM land cover map at 5 km derived from SYNMAP at 1-km-resolution (Jung et al., 2006) and a more precise PFT information in ORCHIDEE land cover maps at 0.5°resolution to determine the C3 or C4 photosynthesis type. In case of the crop PFT, the MIRCA2000 crop map at $\sim 0.08°$-resolution indicates the surface area covered by each crop type, and thus the relevant photosynthesis type, with a finer resolution than in ORCHIDEE and with the monthly variability of the year 2000. The resulting δ_{NPP} varies between 10 and 41‰.

225

δ_{HR} daily maps for the year 2015 are derived from simulations with the above-mentioned ORCHIDEE-MICT emulator. For each grid cell, the daily CO_2 and the corresponding $^{14}CO_2$ emissions from litter respiration and 3 types of soil respiration were aggregated. Their ratio, δ_{HR}, is then interpolated from the ORCHIDEE-MICT grid to the VPRM grid. The resulting δ_{HR}

varies between 22 and 177 ‰.

230

Nuclear $^{14}CO_2$ emissions are simply calculated following Graven and Gruber (2011) based on the annual activity of each reactor, in 2015, reported in Zazzeri et al. (2018). For each reactor, activity data A in $TBq \cdot yr^{-1}$ is converted into ^{14}C production in $kg^{14}C \cdot reactor^{-1} \cdot yr^{-1}$:

$$F_{Nucl}^{14C} = A \times \alpha \times 10^9 \tag{6}$$

235   with $\alpha = R_{std}/0.226$, where $0.226 \ Bq \cdot gC^{-1}$ is the conversion factor from activity to carbon production.

2.3.3   Ignoring ocean fluxes, cosmogenic production, biomass burning emissions and the regional boundary conditions

The impact of uncertainty in the initial condition (at 0:00 on July 1 2015) and at the boundary conditions (at the lateral and top boundaries of the CHIMERE domain) are assumed to be negligible following the results from Santaren et al. (2021): these conditions are thus ignored in the definition of our inversion problem.

240   Regarding the CO_2 (and thus $^{14}CO_2$) ocean fluxes, we also assume that they can be neglected here because the CHIMERE domain is mostly continental.

The cosmogenic production of ^{14}C becomes significant above ~700 hPa, well above the planetary boundary layer (Turnbull et al., 2009), while we are interested in simulating $^{14}CO_2$ concentrations near the ground. Even though we use some high-altitude stations, we can assume that most of the influence from the cosmogenic production at these surface stations comes

245   from the model lateral boundaries and that the cosmogenic production within the modelling domain can be neglected.

CO_2 and $^{14}CO_2$ biomass burning emissions are also neglected since they are generally relatively weak in our modelling domain (especially in the 2-km resolution part of the modelling grid on which the analysis focuses).

2.4   Control Vector

2.4.1   Definition of the Control Vector

250   The control vector is spatialized based on a decomposition of the flux maps into large or administrative regions, large urban areas and large industrial plants.

The study focuses on a set of 23 regions, called "the main area of interest" hereafter: the nine administrative regions of Belgium, Luxemburg, seven administrative regions of the southern Netherlands, three administrative regions in northern France and three administrative regions in western Germany (all comprised in the 2 km × 2 km-resolution zoom of the CHIMERE

255   grid, see Figure 3).
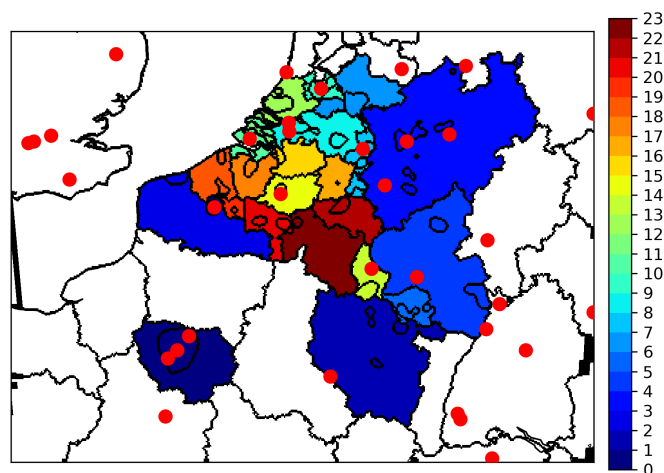
Figure 3. Main area of interest i.e. the 23 administrative regions where major urban areas (contours of the urban areas also represented here) and point sources emissions are controlled separately for anthropogenic emissions in the 2 km × 2 km-resolution zoom of the CHIMERE transport model. The names of these administrative regions are listed in Table 1. Ground-based $^{14}CO_2$ and CO_2 observation sites are also shown (red dots, see Fig. 6, for the network on the whole domain).

Table 1. List of areas of control in the main area of interest and corresponding number of stations in these areas.

Number	Area Name	Number of Stations
1	Île-de-France	3
2	Lorraine	1
3	Nord-Pas-de-Calais	1
4	North Rhine Westphalia	3
5	Rhineland-Palatinate	1
6	Saarland	0
7	Gelderland	0
8	Limburg	1
9	North Brabant	3
10	Utrecht	1
11	Zeeland	1
12	Sheldt (see)	0
13	South Holland	0
14	Luxemburg	1
15	Brabant/Bruxelles	1
16	Anvers	0
17	Limburg	0
18	East Flanders	0
19	West Flanders	0
20	West Hainaut	0
21	East Hainaut	0
22	Liege	0
23	Namur/Luxembourg	0

In this main area of interest, the CO_2 FF emission budgets from major industrial plants (22 plants for which the annual emissions exceed 1 MtC for CO_2, FF_{PS}, see the red dots in Figure 3) and the FF, BF_{wood} and BF_{crop} CO_2 emission budgets from the large urban areas (the 42 urban areas represented in Figure 3) are controlled separately. In each of these 23 regions, the budget of the rest of the FF, BF_{wood} and BF_{crop} CO_2 emissions are controlled separately. Outside this main area of interest, the FF, BF_{wood} and BF_{crop} CO_2 emission budgets of 43 administrative or larger regions are controlled (Fig. 4).
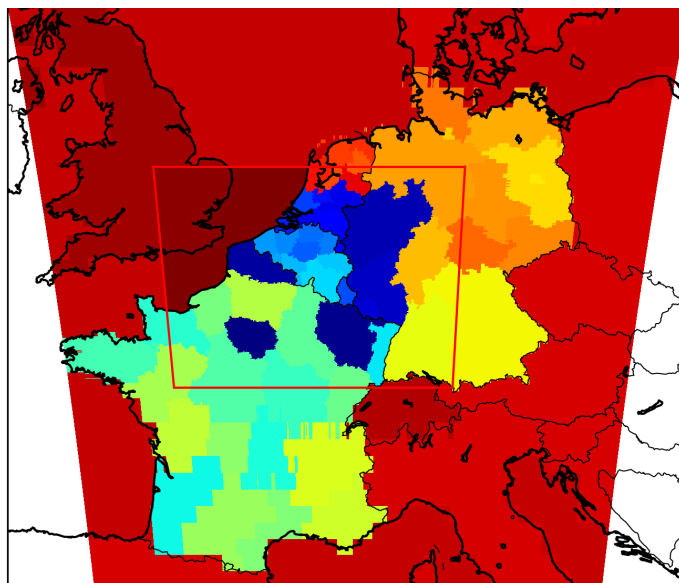
Figure 4. Administrative regions and coarser areas for which the biogenic flux budgets, and the anthropogenic emission budgets (with more details for regions highlighted in Figure 3) are controlled. The red line delimits the 2 km × 2 km-resolution zoom of the CHIMERE transport model.

Single ^{14}C signatures of the BF_{wood} and BF_{crop} fluxes are controlled assuming that they apply over the whole modelling domain. The ^{14}C fluxes from 47 nuclear power plants, across the whole modeling domain, are separately controlled.

Biogenic fluxes and isotopic signatures (NPP, HR and δ_{HR}) are only controlled at the resolution of the 66 administrative regions and larger areas (23 in the main area of interest and 42 outside, Fig. 4), i.e., the spatial resolution of the control vector is nearly the same as for anthropogenic emissions but it does not isolate urban areas and major point sources.

The control vector is actually composed of scaling factors to be applied to maps of local (from plant and urban area) and regional fluxes from the products presented in Section 2.3 over these spatial control areas at a 1-hour temporal resolution except for the ^{14}C signature of the HR, of wood burning and of crops BF emissions which are controlled at the daily scale. The composition of the control vector is summarized in Table 2.

Table 2. Number of parameters in the control vector. The control vector is composed of scaling factors to be applied to budgets and maps of local and regional fluxes from the products presented in Section 2.3 (FF_{PS}, FF_{other}, BF_{crop}, BF_{wood}, NPP, HR, $^{14C}BF_{crop}$, $^{14C}BF_{wood}$, ^{14C}HR and Nucl). This table gives number and type of areas in the control vector: 66 administrative or coarser regions (Reg) defined in Figure 4 and more detailed areas in the main area of interest. PS: point source emissions, UA: large urban area emissions, NUA: non urban area i.e the rest of the region when excluding the UA and Domain: whole domain budget. In a 24h-inversion-window, 24 temporal parameters correspond to 1h temporal resolution and 1 parameter correspond to daily resolution.

		FF_{PS}	FF_{other}	BF_{crop}	BF_{wood}	NPP	HR	$^{14C}BF_{crop}$	$^{14C}BF_{wood}$	^{14C}HR	F_{Nucl}
Spatial	in Main Area of Interest	22 PS	42 UA	42 UA	42 UA	66 Reg	66 Reg	1 Domain	1 Domain	66 Reg	47 PS
		-	23 NUA	23 NUA	23 NUA						
	outside		43 Reg	43 Reg	43 Reg						
	Total	22	108	108	108	66	66	1	1	66	47
Temporal		24	24	24	24	24	24	1	1	1	24
Total		528	2592	2592	2592	1584	1584	1	1	66	1128
Control Vector Size	**1128**										

2.4.2 Prior error covariance matrix B

B is built assuming a 3-hour temporal auto-correlation of the prior uncertainty in hourly budgets for each type of controlled flux. An exponentially decaying function is used to model these temporal correlations: $e^{-d/3}$, where d is the time lag, expressed in hours, between two hourly fluxes. We also assume that there is no correlation of the prior uncertainties in space (between different point sources, urban areas and regions) or between different types of fluxes or isotopic signatures. The standard deviations of the prior uncertainties in control parameters for individual spatial areas at daily scale are set to 30% for FF and BF emissions, to 100% for ^{14}C signatures and to 60% for biogenic fluxes (Table 3). The resulting standard deviations of prior uncertainty in regional 24-h, morning and afternoon budgets of FF emissions in the main area of interest range from 10 to 45% (Table 4).

Table 3. Standard deviations of the prior uncertainties in 24-h budgets of fluxes or in isotopic signatures for each control area.

	FF_{PS}	FF_{other}	BF_{crop}	BF_{wood}	NPP	HR	$^{14C}BF_{crop}$	$^{14C}BF_{wood}$	^{14C}HR	Nucl
Prior uncertainty (%)	30	30	30	30	60	60	100	100	100	100

2.5 Observation vector and corresponding sets of experiments

2.5.1 Satellite observations from an XCO$_2$ spectral imager similar to CO2M

Some of the experiments assimilate pseudo retrievals of XCO$_2$ from a single orbit of a CO2M-like satellite passing over Western Europe at 12:00 UTC. The simulation of these XCO$_2$ satellite observations is based on the simulations of the CO2M 2-km-resolution sampling, with a $\sim$300 km swath, and L2 error statistics in the surface and atmospheric conditions for the

Table 4. Range of standard deviations of the prior uncertainty in regional 24-h, morning and afternoon budgets of FF emissions in the main area of interest. These budgets include the urban areas and point sources within the regions

Prior uncertainty in regional budget (%)	24-h	Morning	Afternoon
Min	10	15	16
Mean	20	29	31
Max	30	43	45

year 2014 from the ESA-PMIF project (Wang et al., 2020; Lespinas et al., 2020). These simulations account for cloud cover

285 which is moderate for the selected orbit (Figure 5). The observation vector is defined by the individual cloud free pixels of the satellite. The extraction of this observation vector from the model outputs is made by selecting the model grid cells in which the centres of these pixels are located. The spatial resolution of our transport model in the area of interest is similar to that of the satellite observation. However, since the satellite ground pixels do not perfectly correspond to the model grid cells in this area, some model grid cells can correspond to several observations. In the coarser part of the model grid, model grid cells

290 correspond to several observations.

XCO_2 is computed from the CHIMERE 3D fields of CO_2 following the rationale of Santaren et al. (2021), notably assuming a constant vertical weighting function:

$$X_{CO_2}(lat, lon) = \frac{\overline{CO_2(P_{top})} \times P_{top} + \int_{P_{top}}^{P_{surf}(lat,lon)} (CO_2(lat,lon,P) \times dP)}{P_{surf}(lat,lon)} \quad (7)$$

where lat and lon are the latitude and the longitude, respectively, P is the atmospheric pressure. P_{surf} is the surface pressure

295 and P_{top} (300 hPa) is the pressure at the top boundary of the model. For pressures lower than P_{top}, we assume that the CO_2 concentrations equal the horizontal average of the top-level mixing ratios in CHIMERE ($\overline{CO_2(P_{top})}$).

2.5.2 Ground-based network

We use a surface network (Fig. 6) of which 113 stations in our modelling domain are located following the scenario proposed by Marshall et al. (2019). This scenario is based on existing continuous CO_2 measurement sites of the Integrated Carbon

300 Observation System (ICOS, https://www.icos-cp.eu/) or other air sampling stations of the National Oceanic and Atmospheric Administration (NOAA) and of the Global Atmosphere Watch Programme of World Meteorological Organization (GAW, https://community.wmo.int/activity-areas/gaw). We assume that these stations have appropriate infrastructures and locations to observe atmospheric CO_2 and $^{14}CO_2$. In order to complement this first network, local meteorological or air quality sampling stations, or local science and engineering faculties were also chosen.

305 The sampling height at these stations ranges between 10 and 344 m above the ground level. We assume that all stations of this network measure simultaneously CO_2 and/or $^{14}CO_2$. Each virtual site is assumed to provide hourly CO_2 data that are assimilated between 10:00 and 17:00 UTC and/or a 7-hour-average sample of $^{14}CO_2$ over 10:00-17:00 UTC, following the

0.40 0.45 0.50 0.55 0.60 0.65 0.70
Averaged error of CO2M cloud free observation (ppm)
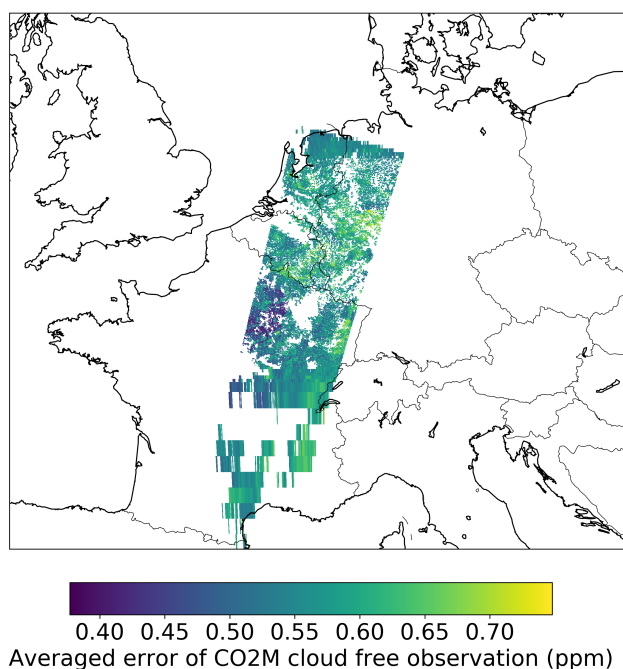
Figure 5. Simulation of the XCO_2 sampling and observation error standard deviation (by IUPB in the ESA-PMIF project) for a selected orbit of the spectral imaging satellite, in parts per million (ppm).

common practice of assimilating data only when the planetary boundary layer (PBL) is well developed (Broquet et al., 2011). The availability of CO_2 7-hour averages when deriving $^{14}CO_2$ 7-hour averages from air samples is ignored.

2.5.3 Observation error covariance matrix R

The matrix **R** combines the uncertainty in the data that are assimilated and the corresponding uncertainty from the observation operator. Here we assume that the uncertainty in the observation operator is dominated by that of the transport model and we ignore temporal and spatial auto-correlations in these uncertainties. For individual data, the standard deviation of the observation error is therefore:

$$\sigma_{obs} = \sqrt{\sigma_{meas}^2 + \sigma_{mod}^2} \tag{8}$$

For satellite observations, σ_{meas} is the uncertainty in the CO2M XCO_2 data as simulated by IUPB. These values are represented in Figure 5. σ_{mod} is taken as 1 ppm for individual data (Basu et al., 2018; Marshall et al., 2019). As described in Section 2.5, since the satellite ground pixels do not perfectly correspond to the model grid cells, some model grid cells can correspond
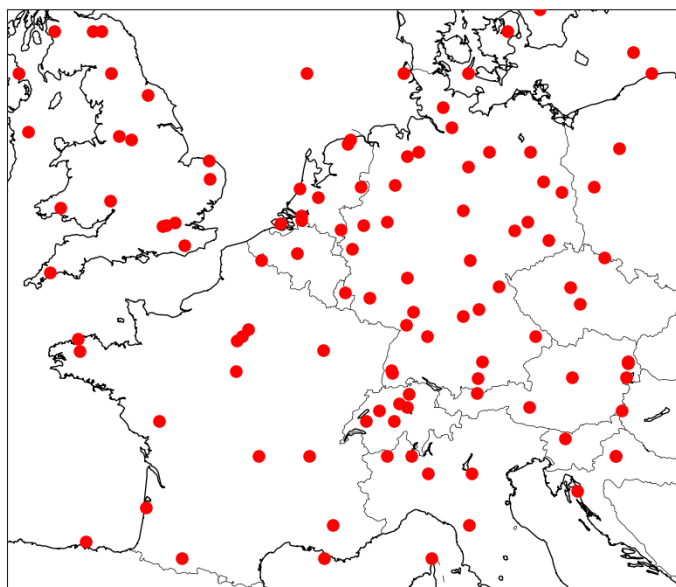
Figure 6. Ground-based $^{14}CO_2$ and CO_2 observation networks. 113 stations located following the scenario proposed by Marshall et al. (2019), based on real or potential observation networks (ICOS, NOAA, GAW, more details in section 2.5.2).

to several observations. We assume that the observation errors are uncorrelated: the aggregation of N observations results in decreasing errors by a factor $1/\sqrt{N}$.

For the near surface CO_2 and $^{14}CO_2$ observations, the configuration of σ_{meas} follows the guidelines of Marshall et al. (2019, Tables 5-1 to 5-3):

- The uncertainty in CO_2 hourly measurements is taken as the target measurement uncertainty, $\sigma_{CO2,meas} = 0.05$ ppm.

- The 1-sigma uncertainty on $^{14}CO_2$ 7-hour data is taken as 200 ppm ‰, based on the following uncertainty propagation:

$$\sigma_{14CO2,meas} = \sqrt{(CO_2 \times \sigma_{\delta 14C,obs})^2 + (\delta_{14C,a} \times \sigma_{CO2,obs}/\sqrt{7})^2} \tag{9}$$

with

- CO_2 the atmospheric concentration set to 400 ppm

- the atmospheric $\delta_{14C,a}$ set to 40 ‰

330   – $\sigma_{CO2,meas}/\sqrt{7}$, the CO_2 measurement uncertainty at the 7-hour scale, assuming that there is no autocorrelation in the CO_2 measurement errors at the hourly scale

     – $\sigma_{\delta14C,meas} = 0.5‰$, the δ_{14C} measurement uncertainty at the 7-hour scale

We use the estimate of the model error from Marshall et al. (2019, Table 5-3): $\sigma_{CO2,model} =$ 1 ppm and $\sigma_{14CO_2,model} =$ 1.26×10^{-12} ppm multiplied by station class multipliers from 1 to 5 depending on the type of station. For $^{14}CO_2$, the conversion

335   was done from ppm to ppm ‰ by multiplying by $1000/R_{std}$. Ignoring auto correlations in the model error at the hourly scale, the model error for 7-hour $^{14}CO_2$ mean concentration data is taken as $1/\sqrt{7}$ times the model error derived at the 1-hour scale.

The range of the resulting error statistics on the different types of data and from the model are reported in Table 5.

Table 5. Data, model, and observation operator 1-sigma uncertainty

Error	Near-surface			Satellite		
	Meas	Model	Obs	Meas	Model	Obs
CO_2 (ppm)	0.05	1 to 5	1 to 5	0.38 to 0.75	1	1.07 to 1.11
$^{14}CO_2$ (ppm ‰)	200	405 to 2025	451 to 2034			

2.5.4   List of experiments

Table 6 provides labels for the different sets of experiments as a function of the sets of pseudo observations that are assimilated, using or combining the satellite data, the surface CO_2 data and/or the surface $^{14}CO_2$ data.

Table 6. List of performed experiments

Inversion System Observations	Name
Satellite XCO2	INV-SAT
Surface CO_2	INV-CO2
Surface $^{14}CO_2$	INV-14C
Satellite XCO2 + Surface CO_2	INV-SAT-CO2
Satellite XCO2 + Surface $^{14}CO_2$	INV-SAT-14C
Satellite XCO2 + Surface CO_2 + Surface $^{14}CO_2$	INV-SAT-CO2-14C

340

2.6   Diagnostics

When analysing the results from the inversions and assessing the potential of the different types of observation networks, we focus on the standard deviation of the prior and posterior uncertainties in flux budgets, and on their relative difference (called uncertainty reduction or UR hereafter):

345   $UR = 1 - \dfrac{\sigma_{post}}{\sigma_{prior}}$ (10)

Hereafter, when analysing temporal budgets of uncertainties, "morning" and "afternoon" are used to designate 6:00-13:00 and 13:00-19:00 UTC, respectively. Our analyses are focused on budgets for regions in the 2-km-resolution area and more particularly in the main area of interest as defined in Figure 3.

To evaluate the impact of ground-based networks, we also define ΔUR_{Test}^{Ref} as the difference between UR for 24-h FF
350   regional budgets, with a test configuration and UR with a reference configuration: $\Delta UR_{Test}^{Ref} = UR_{test} - UR_{Ref}$. In these cases the reference configurations are the ones when assimilating the data from the satellite track, either alone or with CO_2 data from the ground network (INV-SAT and INV-SAT-CO2 see Table 6).

3   Results

3.1   Potential of the satellite observations as a standalone observation system

355   This section describes results when assimilating the data from the satellite track only, i.e. results from the INV-SAT inversion.

3.1.1   General results in the morning

This section focuses on results on morning budgets for which the constraint in the inversion from the satellite observation is the highest. Indeed, the maximal UR for regional morning budgets reaches 32% against 3% for afternoon budgets (Table 7).

Table 7. Best score statistics of the uncertainty reductions and the posterior uncertainty in inversions with and without NEE, for regional 24-h, morning and afternoon FF emission regional budgets. In the main area of interest, these budgets combine emissions from urban areas, large plants and the more diffuse regional sources.

	Uncertainties (%)		INV-SAT	INV-CO2	INV-SAT-CO2	INV-14C	INV-SAT-CO2-14C
With NEE	24-h	UR max	18,4	12.6	23,6	23.0	32,9
		Post min	8,0	8.6	7,5	7.6	6,6
	Morning	UR max	32,4	17.7	37,8	32.7	50,8
		Post min	10,0	12.2	9,2	10.0	7,3
	Afternoon	UR max	2,9	14.7	15,8	10.8	20,5
		Post min	15,6	14.9	14,6	15.1	14,0
Without NEE	24-h	UR max	32.2	26.4	39.2	23.4	40.7
		Post min	6.7	7.2	6.0	7.5	5.8
	Morning	UR max	59.9	36.9	64.4	33.3	66.0
		Post min	5.9	9.3	5.3	9.9	5.0
	Afternoon	UR max	3.9	17.0	17.0	10.8	21.2
		Post min	15.5	13.7	13.4	15.1	13.2

Figure 7 shows the example of a panel of URs from INV-SAT, for the morning budget of CO_2 fluxes, at the scale of point
360   sources to that of regions. The URs for the morning budgets of large industrial plant emissions (FF_{PS}) are significant in
the satellite field of view (FOV, corresponding to the vertical projection of the satellite image on the ground), with values
larger than 50% (Fig. 7a), but is marginal outside this FOV. The northwest direction of the wind on the day of analysis (see
Section 2.2) explains that the observation footprint appears to be slightly extended out of this FOV, in the east, with, for
example, significant UR in the region of Essen. URs are also significant for other fossil fuel emission budgets (FF_{other}) and
365   HR (heterotrophic respiration, as defined above) in the satellite FOV with URs up to 50% and more. The UR for NPP is much
larger than for the other fluxes since this flux is relatively large in July. The UR for BF emissions is generally much smaller
than for the FF emissions. The much weaker level of emission related to BF combustion explains the lack of UR for this type
of fluxes.
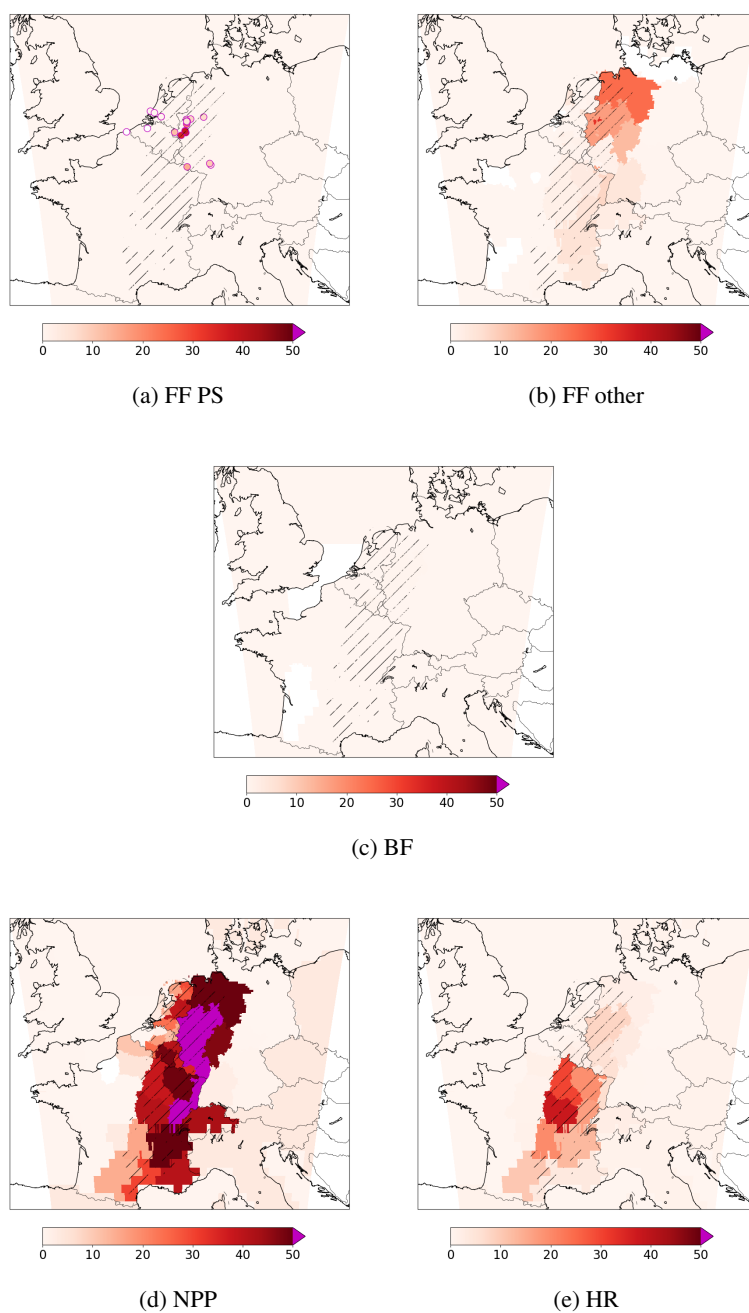
Figure 7. Uncertainty reduction in INV-Sat inversions: for morning budgets of large plants (a, FF_PS, magenta circled dots), other FF (b) and BF (c, crop and wood) emissions (urban area and rest of the region budgets), Net Primary Production (d, NPP) and heterotrophic respiration (e, HR) (regional budgets). Stripes are indicative of the satellite field of view (see Fig. 5 for the full track).

3.1.2 Uncertainties in FF emissions

370 The uncertainty reductions for the 24-hour regional budgets of FF emissions (regional budgets aggregates emissions from urban areas, point source and the rest of the regions hereafter) range from 0 to 18% in the main area of interest (Fig. 9, a, Tab. 7). The URs are similar or rise in a range from 0 to 32% for the regional morning budget (Fig. 8, a and Tab. 7). Larger emission budgets generally lead to larger URs. However, for similar or lower emission budgets (median 8 vs. 14 $kTCO2 \cdot area^{-1} \cdot 24h^{-1}$ respectively), URs are significantly higher for emissions from urban areas than for the other regional emissions (max 18%

375 vs. 10% respectively) since dense emissions areas generate atmospheric signatures with large amplitudes that are easier to filter from other signatures and from the observation noise than more extended but more diffuse emissions areas (Santaren et al., 2021). URs for the afternoon emissions entirely rely on the specification of 3-h temporal auto-correlation in the prior uncertainties in the emissions since these afternoon emissions are not directly seen by the satellite. Consequently, they are low for all types of sources. Figure 8(b) and Table 7 show URs for afternoon regional budgets ranging from 0 to 3%. Overall,

380 the results show contrasting capacities for the monitoring of the FF emissions. The scores of URs result in various levels of precision on the emission estimates, with 8% to 30% posterior uncertainties in 24-hour and regional budgets of FF emissions in the main area of interest (Tab. 7). The lack of constraint outside the satellite FOV and during periods other than the morning confirms the need for complementary data to extrapolate the information derived from the satellite observations in space and time.
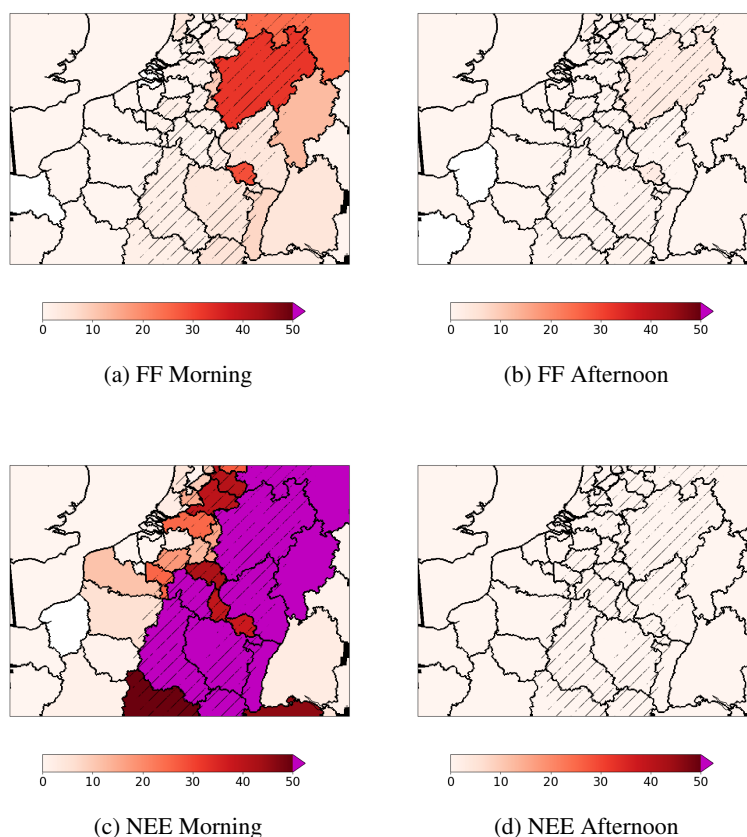
Figure 8. Uncertainty reduction in INV-Sat inversion: for morning (a, c) or afternoon (b, d) budgets of FF, biogenic fluxes (NEE). Stripes are indicative of the satellite field of view (see Fig. 5 for the full track).

3.1.3 Impact of NEE and BF emissions on FF emissions uncertainties

The UR for NEE is much larger than for the FF emissions (Fig. 8, b and c) while the UR for BF emissions is generally much smaller than for the FF emissions (Fig. 7). The problem of the attribution of inferred fluxes to FF emissions, NEE or BF emissions is investigated by conducting sensitivity tests in which the NEE or BF emissions are ignored, i.e. assuming no uncertainty in these fluxes (results when ignoring BF emissions are not shown in the figures and tables for the reasons given below). The INV-SAT experiment ignoring the NEE shows significantly larger URs for the FF regional 24-h budgets (Figure 9), up to 60% in the satellite FOV, for the FF regional morning budget (Table 7, without NEE). This increase of the URs yields posterior uncertainties in 24-h regional budgets which can reach values as low as 6.7% in the satellite FOV (Tab. 7).

INV-Sat 24-h FF budget
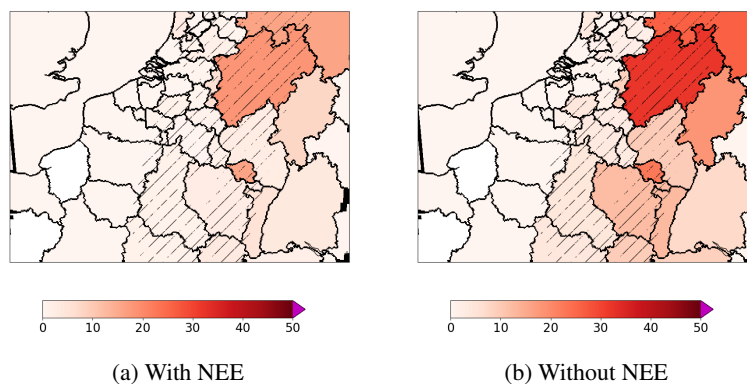
Figure 9. Uncertainty reduction in INV-Sat inversion with (a) and without (b) NEE, for 24-h budgets of FF emissions. Stripes are indicative of the satellite field of view (see Fig. 5 for the full track).

The sensitivity of INV-SAT experiment to the inclusion of BF emissions shows a very weak impact of BF emissions on the UR for FF emissions (not shown) even though the spatial distribution of these two types of emissions are strongly correlated.

395 This is directly attributed to the weak amplitude of BF emissions compared to FF emissions. Typically, the posterior uncertainty in the FF emissions (6 to 30 % of the 24-h BF + FF emission budget) is much larger than the prior uncertainty in BF emissions (0 to 7% of the 24-h BF + FF emission budget).

3.2 Potential of the ground-based hourly CO_2 network

This section evaluates the impact of co-assimilating data from the ground-based hourly CO_2 network and the potential com-

400 plementarity between the satellite and the CO_2 ground-based hourly observations. This evaluation is based on the analysis of INV-CO2 and INV-SAT-CO2 and comparisons with the results from INV-SAT.

3.2.1 General results for the FF emissions

INV-CO2 (Fig. 10) reveals the limited role of the horizontal atmospheric transport near the surface to propagate URs from regions with several measurement stations to other ones. URs of more than 4%, median at 12% and maximum at 13%, for 24-h

405 budgets can be achieved in regions with 3 stations, like Île-de-France (Reg. 1, 12%), and North Rhine-Westphalia (Reg.4, 13%) in the main area of interest (see also Fig. A1), or in regions with more stations outside this area like southeast England (10%) and Baden-Württemberg (26%) which have 5 stations. However, the UR can also be much lower in regions with many stations, e.g. for Lower-Saxony-and-Bremen which has 5 stations but a 4% UR. UR in regions with 1 or 2 stations range between 0% and 6%. The URs are generally below 1% for other regions. These URs reach lower or comparable values than in the INV-

410 SAT experiment in the main area of interest (Fig.A1, Tab 7). However, outside the main area of interest, Baden-Württemberg reaches a higher value than the largest one with the INV-SAT experiment (Rhineland-Palatinate, Reg. 5, 18%).
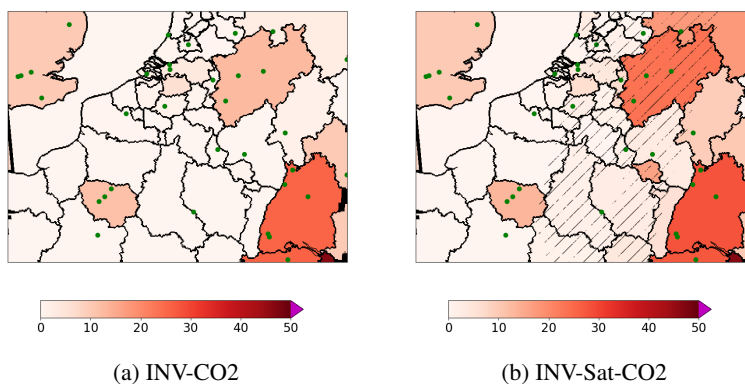
24-h FF budget
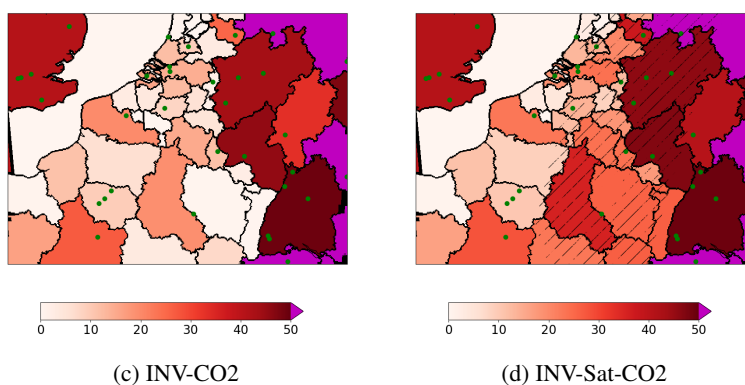
Figure 10. Uncertainty reduction in INV-CO2 (a, c) and INV-Sat-CO2 (b, d) inversions: for 24-h budgets of FF emissions and biogenic fluxes (NEE). Stripes are indicative of the satellite field of view. Green dots indicate the ground stations.

Of note is that the highest UR in the whole inversion domain (47% for 24-hour budgets and 56% for morning budgets) corresponds to large regions of the coarse resolution area of the transport model (not represented in Fig. 10). This result is primarily driven by the optimistic extrapolation of information from the sites to the coarse model grid cells and further to the whole extent of the control areas in which they stand. This optimistic bias from the inversion configuration actually results in representation and aggregation errors when conducting experiments with real data (Kaminski et al., 2001; Wang et al., 2017). It justifies and supports the use of the finer resolution control vector in the main area of interest, and the focus of our analysis on the 2-km resolution model subdomain. Unlike satellite data alone in INV-SAT, the ground-based CO_2 data constrains both afternoon and morning emission estimates, with URs of 4 to 18% and 4 to 15% respectively for morning and afternoon regional budgets of FF emissions in the regions with 3 or more stations (Fig. A3 and A4).

3.2.2 Co-assimilation of the satellite observations

Only one region of the 2-km resolution model subdomain with 3 stations is located in the satellite FOV: North Rhine-Westphalia. When comparing the URs for the 24-h regional budgets of FF emissions from INV-SAT-CO2 to that from INV-SAT and INV-CO2 (Tab. 8, Fig. A1) two significant changes can be seen. The first one is the decrease of 5% of the posterior uncertainty for this region, i.e. less than the UR for this region in INV-CO2 (12%). The second one is the increase of UR for the regions outside the satellite FOV with more than 3 ground-based stations from nearly 0% to values that are nearly the same as in INV-CO2. The URs at 24-h scale in INV-SAT-CO2 are smaller than the addition of URs in INV-SAT and INV-CO2 experiment (Fig. 11 and Fig. A1)

Table 8. CO_2 or/and $^{14}CO_2$ ground network impact in addition to satellite observation: ΔUR_{Test}^{Ref} on 24-h, Morning and Afternoon FF regional budgets, Maximal value on the AOI (column MAX), and value of the 2 most impacted area (Île-de-France and North Rhine Westphalia, column).

| | Test | Ref | $\Delta UR_{Test}^{Ref}(\%)$ | | | |
			MAX	MEAN	Île-de-France	North Rhine Westphalia
Daily	INV-SAT-CO2	INV-SAT	13,3	1,6	13,3	5,2
	INV-SAT-14C	INV-SAT	14,6	2,5	14,6	12,7
	INV-SAT-CO2-14C	INV-SAT	20,8	3,3	20,8	14,5
	INV-SAT-CO2-14C	INV-SAT-CO2	9,3	1,8	7,5	9,3
Morning	INV-SAT-CO2	INV-SAT	12,7	1,7	12,7	5,4
	INV-SAT-14C	INV-SAT	16,5	2,7	11,9	16,5
	INV-SAT-CO2-14C	INV-SAT	19,2	3,7	19,2	18,4
	INV-SAT-CO2-14C	INV-SAT-CO2	13	2,1	6,5	13
Afternoon	INV-SAT-CO2	INV-SAT	15,8	1,2	15,8	6,4
	INV-SAT-14C	INV-SAT	10,8	1	10,8	5,6
	INV-SAT-CO2-14C	INV-SAT	20,5	1,8	20,5	10
	INV-SAT-CO2-14C	INV-SAT-CO2	4,7	0,5	4,7	3,6
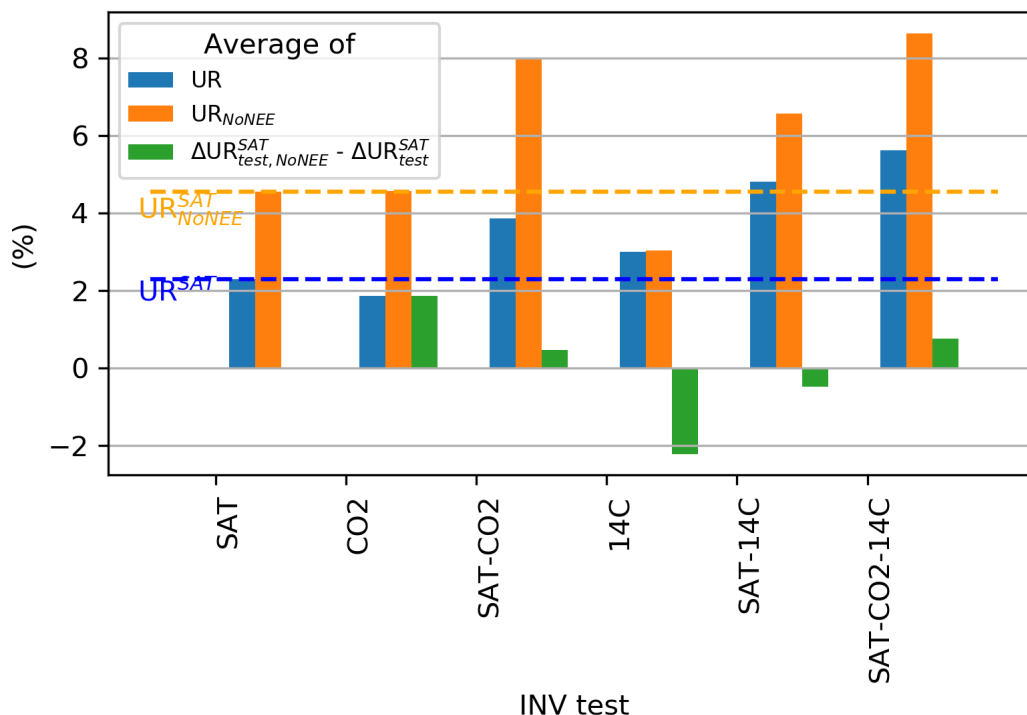
Figure 11. Average on the main area of interest of the UR on 24-h FF regional budgets in a set of inversion configurations, with (blue) and without (orange) NEE and average of the difference between ΔUR_{test}^{SAT} with and without NEE (green). Negative values highlight an increase of the additional observation network potential when NEE is taken into account.Positive values highlight a decrease of the additional observation network potential when NEE is taken into account. High absolute values highlight strong NEE impact.

The ground-based CO_2 data constrains both afternoon and morning emission estimates, with URs of 3 to 30% and of 1 to
430 27% respectively for morning and afternoon regional budgets of FF emissions in the regions with three or more stations (data not shown). The comparison between results for afternoon budgets of the FF emissions from INV-SAT-CO2 and INV-SAT shows again, in INV-SAT-CO2, an increased UR that is smaller than the sum of the URs obtained in INV-SAT and INV-CO2 (Tab. 7). Combining the satellite data with the afternoon data from the ground network does not increase the ability to extrapolate the spatially widely spread information from these satellite data to the afternoon.

435 **3.2.3 Impact of NEE and BF emissions on FF emissions uncertainty**

INV-CO2 and the results of INV-SAT-CO2 outside the FOV of the satellite show different situations regarding the comparison between UR for NEE and FF emissions (Fig. 10). In regions with large cities and industrial plants (like the Paris area and Baden-Württemberg), the URs for NEE are smaller than that for FF as in INV-SAT. However, in other regions, the signal at the surface stations is dominated by the signature of the biogenic fluxes and URs for NEE are larger than that for FF emissions.

440 Due to the relatively weak signal from BF emissions, the URs for these emissions are much smaller than that for FF emissions (less than 3%, less than 0.1% on average) in INV-CO2.

The impact of the attribution problem when using the surface CO_2 network is quantified, here again, by conducting sensitivity tests in which NEE is ignored (Fig. 11 and Tab. 7). As the surface network has many stations mostly sensitive to the NEE signal, it is expected to support the distinction between NEE and FF emissions in the inversion, even if the stations measure

445 CO_2 only. In inversions INV-CO2, the UR for FF emissions is higher when ignoring the NEE, reaching a range between 18 and 46% for 24-h budgets in the regions with more than 3 stations. However, the comparison between results from INV-SAT-CO2 and INV-SAT when ignoring these fluxes hardly demonstrates a potential of the surface CO_2 network to reduce the problem of attribution between FF emissions and other fluxes (Fig. 11). Figures 11 show $\Delta\text{UR}_{SAT-CO2,NoNEE}^{SAT}$ larger than $\Delta\text{UR}_{SAT-CO2}^{SAT}$ on average, i.e adding the CO_2 network when ignoring the NEE yields a larger increase of the UR than when

450 accounting for NEE. This is linked to the smaller UR associated with CO_2 data when accounting for NEE. There is a lack of indirect feedback on the UR for FF emissions from the lowering of uncertainties in NEE when complementing the satellite data with CO_2 data. However the results for each area taken independently show somewhat contrasting results (Fig. 12) with $\Delta\text{UR}_{SAT-CO2,NoNEE}^{SAT}$ lower than $\Delta\text{UR}_{SAT-CO2}^{SAT}$ in some regions.
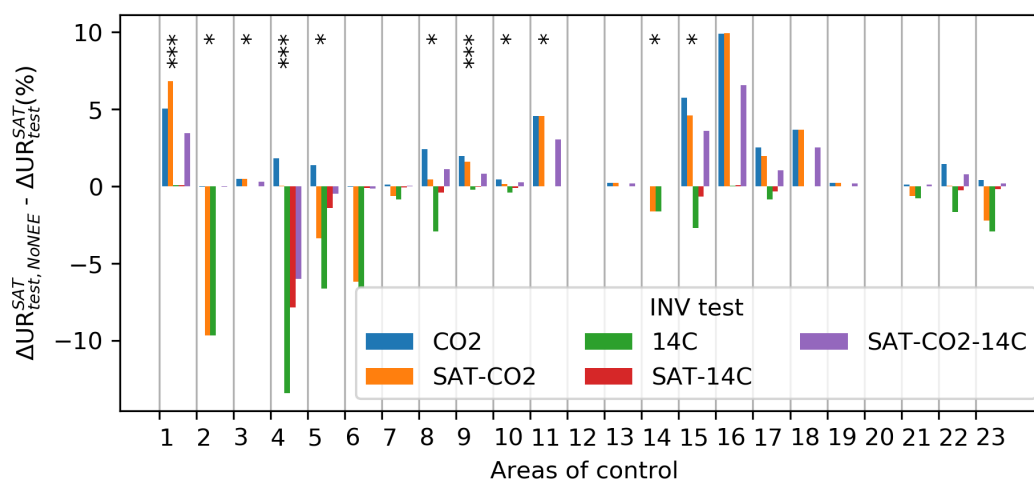
Figure 12. Impact of the NEE on the ground network capability on the top of the satellite observation for each area of control in the main area of interest: differences between $\Delta\text{UR}_{test}^{SAT}$ on 24-h FF regional budgets, with and without NEE. Negative values highlight an increase of the additional observation network potential when NEE is taken into account. Positive values highlight a decrease of the additional observation network potential when NEE is taken into account. High absolute values highlight strong NEE impact. The number of stars indicates the number of stations in each controlled area. The areas are listed in Appendix 1.

Regarding BF emissions, the results are similar to that described in section 3.1, i.e a very weak impact of BF emissions

455 on the UR for FF emissions. With INV-SAT-CO2 the posterior uncertainties in FF emissions (7 to 30% of the 24-h BF + FF emission budget) are much larger than the prior uncertainty in BF emissions (0 to 7% of the 24-h BF + FF emission budget).

3.3 Potential of the ground-based $^{14}CO_2$ network

This section evaluates the impact of co-assimilating data from the ground-based 7-h-average $^{14}CO_2$ network and the potential complementarities between the satellite and hourly-CO_2, 7-h-average $^{14}CO_2$ ground-based observations. This evaluation is based on the analysis of INV-14C and INV-SAT-CO2-14C and comparisons with the results from INV-CO2 and INV-SAT-CO2.

3.3.1 General results for the FF emissions

The spatial distribution of the regional URs for 24-h, morning or afternoon budgets when using surface 7-h-average $^{14}CO_2$ data alone is similar to that when using hourly-CO_2 surface data only (Fig. 13). These URs are very low for regions with less than 2 stations (<7%) and range between 12 to 34% for the morning budgets and between 4 to 14% for the afternoon budgets for regions with more than 3 sites. The URs on daily and morning budgets are larger in INV-14C (Tab. 7, Fig. A2 and A5), i.e. when using the sampling of $^{14}CO_2$ representative of 7-h-averages of the concentrations, than in INV-CO2 (Tab. 7, Fig. A1 and A3), when using 7 hourly CO_2 data at each site. However, the URs on afternoon budgets are smaller in INV-14C than in INV-CO2. In most regions these differences remain relatively small except in Region 4, North Rhine Westphalia, with up to 15 percentage points difference from the morning budget. The higher potential of $^{14}CO_2$ data (7-hour averages) than hourly CO_2 data to filter the signal from FF emissions, if both were measured at the same temporal resolution, is balanced by the finer temporal resolution of the hourly CO_2 continuous measurements. The hourly CO_2 data's finer temporal resolution helps capture the high frequency patterns of the signal from FF emissions.

24-h FF budget
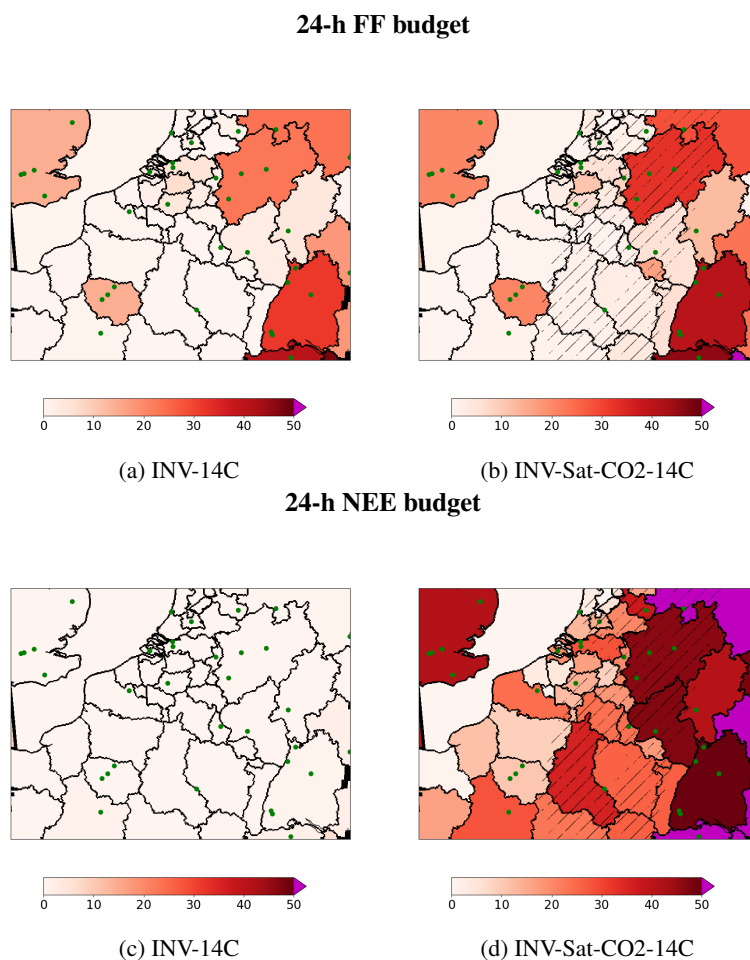
Figure 13. Uncertainty reduction in INV-14C (a) and INV-Sat-CO2-14C (c) inversions: for 24-h budgets of FF emissions (a, b, c) and biogenic fluxes (NEE, d, e, f). Stripes are indicative of the satellite field of view (see Fig. 5 for the full track). Green dots indicate the ground stations.

3.3.2 Co-assimilation of the satellite and surface hourly-CO$_2$ observations

475 The fact that the URs when combining two networks is smaller than the sum of the URs when using each of these networks shown when comparing INV-SAT, INV-CO2 and INV-SAT-CO2, also applies when adding the surface network i.e. when comparing e.g. INV-SAT-14C to INV-SAT and INV-14C or INV-SAT-CO2-14C to INV-SAT-CO2 and INV-14C. The combination of 7-h-average ^{14}CO$_2$ data with other types of data does not lead to further synergies of the advantages for each network: the spatial extent of the satellite observation, the temporal coverage of the ground-based networks, the temporal resolution of the

480 hourly-CO$_2$ surface network, and the higher sensitivity to FF emissions of the 7-h-average ^{14}CO$_2$ network. In North Rhine-Westphalia, where the configuration is favourable, with 3 stations in the satellite FOV, the UR for the daily budget increases from 18% with INV-SAT to 33% with INV-SAT-CO2-14C (Fig. 13, Reg. 4). This configuration leads to 6.6% posterior un-

certainty. In Île-de-France (Reg. 1) outside the satellite FOV and with 3 stations, the UR reaches 21% in INV-SAT-CO2-14C, reaching 18% posterior uncertainty. In Saarland (Reg. 6), in the satellite FOV and without stations, the UR remains similar in

485 INV-SAT-CO2-14C as in INV-SAT, 17%, corresponding to 15% posterior uncertainty.

3.3.3 Impact of $^{14}CO_2$ sources: nuclear emissions, NEE and BF emissions

The impact of nuclear emissions in the inversions assimilating $^{14}CO_2$ data is analysed by conducting experiments where these emissions are ignored. The comparison of INV-14C experiments with and without nuclear emissions shows a decrease of the URs, in the range of 0-1.7 percentage points (Fig. A7, a), when these 14C emissions are taken into account. In the main area of

490 interest, the most impacted areas are the Zeeland, Brabant/Bruxelles, Anvers and Flanders regions where the stations are close to nuclear power plants (Fig. A7, b). Outside the main area of interest, Baden-Wurttemberg is also strongly impacted, with up to 9% points difference.

Concerning the impact of NEE, in INV-14C, the URs for FF emissions in the regions with more than 3 stations are higher when ignoring the NEE, reaching a range between 15 and 33% for 24-h budgets. The comparison of the experiments INV-14C

495 with and without NEE shows a much smaller impact of NEE on the URs for FF emissions than in experiments INV-CO2 or INV-SAT, which confirms the much smaller sensitivity of $^{14}CO_2$ data to NEE than CO_2 data. An interesting consequence is that, on average, ΔUR_{14C}^{SAT}, $\Delta UR_{SAT-14C}^{SAT}$ (Fig. 11) or $\Delta UR_{SAT-CO2-14C}^{SAT-CO2}$ (not shown) are slightly larger when accounting for the NEE than when ignoring them. The potential of the $^{14}CO_2$ network to complement the satellite observation is higher when NEE is accounted for, while section 3.2 showed more contrasting results for the surface CO_2 network. This increase of

500 the impact of the $^{14}CO_2$ network when accounting for NEE is however relatively small, reaching its maximum in the region North Rhine-Westphalia, which has 3 stations, and where the posterior uncertainty decrease for the 24-h regional budgets of FF emissions from INV-SAT to INV-SAT-14C is 15%.

4 Discussion and Conclusions

4.1 Configuration of the inversion

505 Several caveats should be raised for the interpretation of these results. Part of the lack of amplification of the impact from the different observation subsystems when combining them could be due to our set-up of the prior uncertainties in which we ignore spatial correlations and assume that the temporal correlations are relatively low. These assumptions are conservative and, we believe, safer, in a context where the correlations of uncertainties in current inventories are still poorly characterized and, since they are probably highly complex and far from isotropic, homogeneous, decreasing with distance or time. For

510 instance, distant plants or cities can have more similar processes than close ones, and the emissions and their underlying processes can vary rapidly depending on the time, weather, or socio-economic drivers... Inversions assuming large temporal and spatial correlations in the prior uncertainties in inventories would indicate a stronger ability to extrapolate the information from atmospheric data but would be overly optimistic.

Our model of the uncertainty in the atmospheric transport is relatively simple here: a Gaussian distribution without any spatial and temporal correlations, as traditionally done in atmospheric inversions (Santaren et al., 2021). Complex modelling errors could actually shift or modify the patterns of the atmospheric signature of the FF emissions, which could increase the weight of the attribution problem, and thus the potential of the combination between satellite and surface data. However, very dense surface networks would be needed to support the identification and adjustment of transport errors.

The results demonstrate the need for a complex simulation of the CO_2 and $^{14}CO_2$ transport, taking into account the diversity of $^{14}CO_2$ sources and sinks, and more realistic than the common simplification which consists of representing only the dilution of radiocarbon-free FF CO_2 emissions. This and an inversion system at high resolution is more suitable for assessing the real ability to extrapolate information from the $^{14}CO_2$ atmospheric data. However, given its high spatial and temporal resolution, the analytical inversion framework used here can hardly be run over several days, because the size of the matrices to be inverted would become too large. Therefore, inversions have been run for one day only, on July 1 2015 i.e. for very specific atmospheric conditions and biogenic fluxes. In summer the biogenic fluxes are relatively high. Tests over different days, e.g. in winter, could bring a more precise characterization of the complementarity of in situ networks with satellite data, but the primary focus of this study was to investigate the problem of the separation between the biogenic fluxes and FF emissions. By limiting the inversion window to a single day, we avoid analyzing to which extent the temporal correlations of the uncertainties in the FF CO_2 emission inventories allow for cross-referencing the information of data from different days. This assessment should rely on a strong knowledge on the structures of uncertainties in the FF emissions, which is still incomplete, as illustrated above, even though efforts have been conducted to improve this issue (Wang et al., 2020; Super et al., 2020).

Finally our study tested a surface network roughly corresponding to the extension of a continental network like ICOS for the monitoring of regional FF emission budgets. The deployment of networks dedicated to specific cities with stations around and within the urban areas (Wu et al., 2016) would correspond to a different strategy and could result in different conclusions for the monitoring of city emissions.

4.2 Insights from the results

The results presented here raise contrasting conclusions regarding the potential of the combination between the satellite observation and the surface networks. The satellite observation, as a stand-alone system, can yield estimates of the regional budgets of FF emissions in the morning corresponding to its days of overpass with uncertainties down to 10% (prior 15%, UR 32%) in its FOV. However, it does not provide direct information on emissions during the afternoon or during the night, and it hardly provides information on plants, cities and regions outside its FOV. Furthermore, previous publications (Broquet et al., 2018; Wang et al., 2020; Lespinas et al., 2020; Kuhlmann et al., 2019) have shown that, even with a CO2M constellation of three or more satellites, the number of overpasses producing local images with low cloud cover is limited each year. The data gaps are not random over time and hamper the estimation of annual budgets or their anomalies, as illustrated in the case of the "Great Lockdown" (Chevallier et al., 2020). The need for complementary sources of information to derive daily to annual budgets is thus critical.

The problem of attributing the inferred CO_2 fluxes to specific emission and absorption types appears to be nearly secondary compared to that of the satellite observation precision but our results confirm that there is a significant impact of the uncertainty in the NEE for the estimate of FF emissions. The uncertainty in BF emissions does not appear to have a large impact on the

550   estimate of FF emissions but this is related to the fact that the posterior uncertainty in FF emissions remains larger than the prior uncertainty in BF emissions i.e. to the relatively low level of BF emissions compared to the typical uncertainties in FF emissions at regional to local scales. If the goal is to achieve higher precision estimates of the FF emissions than those obtained with the present configuration, for example with higher precision spaceborne instruments, and if the share of BF emissions increases in the future, the uncertainty in BF emissions would probably become a major problem due to the strong correlation

555   between the spatial distributions of FF and BF emissions. The problem of attribution to NEE fluxes would also increase with this goal of higher precision estimates of the FF emissions in the future.

Surface $CO_2/^{14}CO_2$ networks can help further decrease the uncertainty in the FF emissions estimates when combined with satellite observations. In North Rhine-Westphalia, the addition of CO_2 and $^{14}CO_2$ stations decreases the posterior uncertainty in daily regional emissions from 8% with the satellite alone to 6.6% However, relatively dense networks close to highly

560   emitting areas are needed to support such a decrease. The isolated stations far from the urban areas do not provide a direct strong constraint for the estimate of the FF emissions, nor a significant indirect constraint for this estimate by solving for the attribution problem. Our results suggest that surface CO_2 and/or $^{14}CO_2$ measurements in support of the FF emission monitoring should be targeting FF emission areas directly rather than the surrounding NEE. Both hourly CO_2 and daily $^{14}CO_2$ data can provide useful information on the FF emissions, the former catching the signature of these emissions at high frequency and the

565   latter being much less sensitive to the uncertainty in the NEE.

Overall, the results illustrate a decrease of the potential of each observation subsystem rather than an amplification of these potentials when combining them together into a large observation system with satellite and surface data. This is the natural consequence of the asymptotic convergence of the precision of inversions towards some low value when adding observations. Tn our experiments, crossing the spatial extent of the satellite observation, the temporal coverage of the ground-based networks,

570   the temporal resolution of the CO_2 surface network, and the higher sensitivity to FF emissions of the $^{14}CO_2$ network does not lead to the expected synergy with wide spatio-temporal coverage of the FF emissions at high resolution. There is a lack of new extrapolation of information from the combination of observation subsystems. This may be due to the specificities of the attribution and extrapolation problems in our inversion case.

Therefore, these results support the deployment of very dense $CO_2/^{14}CO_2$ surface networks to support the satellite obser-

575   vation, with at least three sites per European administrative region. The large-scale deployment of such dense networks is probably unaffordable in the coming decade, but some regions are now equipped with many stations and in some locations, the complementarity between satellite and surface networks could thus be demonstrated. Frequent (up to daily) samplings of $^{14}CO_2$ would be needed to ensure $^{14}CO_2$ data can bring information on FF emissions more precise than that of hourly CO_2 measurements.

580 *Author contributions.* 1) writing process: mainly EP, GB, FC with inputs from all co authors, 2) System and experiment design: EP, GB, FC, YW, PC, DS, 3) Implementation: EP, 4) support in development and use of data: AB, IP, FMB, JM 5) Analysis: mainly EP, GB, FC with feedbacks from all co authors

Competing interests. The authors declare that they have no conflict of interest.

Acknowledgements. This study has been funded by the European Union's Horizon 2020 research and innovation programme under grant
585 agreements No 776186 (CO_2 Human Emissions project) and 958927 (Prototype system for a Copernicus CO_2 service). This work was granted access to the HPC resources of TGCC under the allocations A0090102201 made by GENCI. We wish to thank Michael Buchwitz and Maximilian Reuter (IUP-UB), as well as Yasjka Meijer and Armin Loescher from from ESA for providing the CO2M XCO2 L2 simulations, which were generated in the study funded by the European Space Agency under Contract No 4000120184. We also thank all the CHE partners and particularly Hugo Denier van der Gon (TNO) for providing the anthropognic CO_2 inventories, Julia Marshall (MPI-BGC)
590 for providing the biogenic CO_2 fluxes and Tonatiuh Nuñez Ramirez (MPI-BGC) for designing the ground-based network scenario, in the context of WP4 of CHE.

References

Agusti-Panareda, A.: The CHE Tier1 Global Nature Run, Tech. rep., CO2 Human Emissions, H2020 European Project, https://www.che-project.eu/sites/default/files/2018-07/CHE-D2.2-V1-0.pdf, 2018.

Basu, S., Miller, J. B., and Lehman, S.: Separation of biospheric and fossil fuel fluxes of CO2 by atmospheric inversion of CO2 and 14CO2 measurements: Observation System Simulations, Atmos. Chem. Phys., 16, 5665–5683, https://doi.org/10.5194/acp-16-5665-2016, number: 9 Reporter: Atmos. Chem. Phys., 2016.

Basu, S., Baker, D. F., Chevallier, F., Patra, P. K., Liu, J., and Miller, J. B.: The impact of transport model differences on CO_2 surface flux estimates from OCO-2 retrievals of column average CO_2, Atmospheric Chemistry and Physics, 18, 7189–7215, https://doi.org/10.5194/acp-18-7189-2018, 2018.

Berchet, A., Sollum, E., Thompson, R. L., Pison, I., Thanwerdas, J., Broquet, G., Chevallier, F., Aalto, T., Berchet, A., Bergamaschi, P., Brunner, D., Engelen, R., Fortems-Cheiney, A., Gerbig, C., Groot Zwaaftink, C. D., Haussaire, J.-M., Henne, S., Houweling, S., Karstens, U., Kutsch, W. L., Luijkx, I. T., Monteil, G., Palmer, P. I., van Peet, J. C. A., Peters, W., Peylin, P., Potier, E., Rödenbeck, C., Saunois, M., Scholze, M., Tsuruta, A., and Zhao, Y.: The Community Inversion Framework v1.0: a unified system for atmospheric inversion studies, Geoscientific Model Development, 14, 5331–5354, https://doi.org/10.5194/gmd-14-5331-2021, 2021.

Broquet, G., Chevallier, F., Rayner, P., Aulagnier, C., Pison, I., Ramonet, M., Schmidt, M., Vermeulen, A. T., and Ciais, P.: A European summertime CO2 biogenic flux inversion at mesoscale from continuous in situ mixing ratio measurements, Journal of Geophysical Research: Atmospheres, 116, https://doi.org/https://doi.org/10.1029/2011JD016202, 2011.

Broquet, G., Bréon, F.-M., Renault, E., Buchwitz, M., Reuter, M., Bovensmann, H., Chevallier, F., Wu, L., and Ciais, P.: The potential of satellite spectro-imagery for monitoring CO2 emissions from large cities, Atmos. Meas. Tech., 11, 681–708, https://doi.org/10.5194/amt-11-681-2018, number: 2 Reporter: Atmos. Meas. Tech., 2018.

Chevallier, F., Zheng, B., Broquet, G., Ciais, P., Liu, Z., Davis, S. J., Deng, Z., Wang, Y., Bréon, F.-M., and O'Dell, C. W.: Local Anomalies in the Column-Averaged Dry Air Mole Fractions of Carbon Dioxide Across the Globe During the First Months of the Coronavirus Recession, Geophysical Research Letters, 47, e2020GL090 244, https://doi.org/https://doi.org/10.1029/2020GL090244, 2020.

Ciais, P., Crisp, D., Denier van der Gon, H. A. C., Enge-len, R., Heimann, M., Janssens-Maenhout, G., and Rayner, P., a. S. M.: Towards a European Operational Observing System to Monitor Fossil CO2 emissions, Tech. rep., European Commission Directorate-General for Internal Market, Industry, Entrepreneurship and SMEs Directorate I – Space Policy, Copernicus and Defence, Brussels, Belgium, https://doi.org/10.2788/52148, 2015.

Ciais, P., Wang, Y., Andrew, R., Bréon, F. M., Chevallier, F., Broquet, G., Nabuurs, G. J., Peters, G., McGrath, M., Meng, W., Zheng, B., and Tao, S.: Biofuel burning and human respiration bias on satellite estimates of fossil fuel CO2 emissions, Environmental Research Letters, 15, 074 036, https://doi.org/10.1088/1748-9326/ab7835, 2020.

Degens, E. T.: Biogeochemistry of Stable Carbon Isotopes, pp. 304–329, Springer Berlin Heidelberg, Berlin, Heidelberg, https://doi.org/10.1007/978-3-642-87734-6_14, 1969.

Denier van der Gon, H. A. C., Kuenen, J. J. P., Janssens-Maenhout, G., Döring, U., Jonkers, S., and Visschedijk, A.: TNO_CAMS high resolution European emission inventory 2000–2014 for anthropogenic CO_2 and future years following two different pathways, Earth System Science Data Discussions, pp. 1–30, https://doi.org/https://doi.org/10.5194/essd-2017-124, publisher: Copernicus GmbH, 2017.

ESA: ESA Annual Report 2015, Tech. rep., ESA, 2015.

Farquhar, G. D., Ehleringer, J. R., and Hubick, K. T.: Carbon Isotope Discrimination and Photosynthesis, Annual Review of Plant Physiology
and Plant Molecular Biology, 40, 503–537, https://doi.org/10.1146/annurev.pp.40.060189.002443, 1989.

Fortems-Cheiney, A., Pison, I., Broquet, G., Dufour, G., Berchet, A., Potier, E., Coman, A., Siour, G., and Costantino, L.: Variational
regional inverse modeling of reactive species emissions with PYVAR-CHIMERE-v2019, Geoscientific Model Development, 14, 2939–
2957, https://doi.org/10.5194/gmd-14-2939-2021, 2021.

Graven, H. and Gruber, N.: Continental-scale enrichment of atmospheric 14CO2 from the nuclear power industry: Potential impact on the
estimation of fossil fuel-derived CO2, Atmospheric Chemistry and Physics Discussions, 11, 14 583–14 605, https://doi.org/10.5194/acpd-
11-14583-2011, reporter: Atmospheric Chemistry and Physics Discussions, 2011.

Graven, H., Allison, C. E., Etheridge, D. M., Hammer, S., Keeling, R. F., Levin, I., Meijer, H. A. J., Rubino, M., Tans, P. P., Trudinger,
C. M., Vaughn, B. H., and White, J. W. C.: Compiled records of carbon isotopes in atmospheric CO2; for historical simulations in CMIP6,
Geoscientific Model Development, 10, 4405–4417, https://doi.org/10.5194/gmd-10-4405-2017, number: 12 Reporter: Geoscientific Model
Development, 2017.

Guimberteau, M., Zhu, D., Maignan, F., Huang, Y., Yue, C., Dantec-Nédélec, S., Ottlé, C., Jornet-Puig, A., Bastos, A., Laurent, P., Goll,
D., Bowring, S., Chang, J., Guenet, B., Tifafi, M., Peng, S., Krinner, G., Ducharne, A., Wang, F., Wang, T., Wang, X., Wang, Y., Yin,
Z., Lauerwald, R., Joetzjer, E., Qiu, C., Kim, H., and Ciais, P.: ORCHIDEE-MICT (v8.4.1), a land surface model for the high latitudes:
model description and validation, Geoscientific Model Development, 11, 121–163, https://doi.org/10.5194/gmd-11-121-2018, publisher:
Copernicus GmbH, 2018.

Hammer, S. and Levin, I.: Monthly mean atmospheric D14CO2 at Jungfraujoch and Schauinsland from 1986 to 2016,
https://doi.org/10.11588/data/10100, 2017.

IPCC: 2019 Refinement to the 2006 IPCC Guidelines for National Greenhouse Gas Inventories, Tech. rep., Calvo Buendia, E., Tanabe, K.,
Kranjc, A., Baasansuren, J., Fukuda, M., Ngarize, S., Osako, A., Pyrozhenko, Y., Shermanau, P. and Federici, S. (eds), 2019.

Jung, M., Henkel, K., Herold, M., and Churkina, G.: Exploiting synergies of global land cover products for carbon cycle modeling, Remote
Sensing of Environment, 101, 534–553, https://doi.org/https://doi.org/10.1016/j.rse.2006.01.020, 2006.

Kaminski, T., Rayner, P. J., Heimann, M., and Enting, I. G.: On aggregation errors in atmospheric transport inversions,
Journal of Geophysical Research: Atmospheres, 106, 4703–4715, https://doi.org/https://doi.org/10.1029/2000JD900581, _eprint:
https://agupubs.onlinelibrary.wiley.com/doi/pdf/10.1029/2000JD900581, 2001.

Kuhlmann, G., Broquet, G., Marshall, J., Clément, V., Löscher, A., Meijer, Y., and Brunner, D.: Detectability of CO_2 emission plumes of
cities and power plants with the Copernicus Anthropogenic CO_2 Monitoring (CO2M) mission, Atmospheric Measurement Techniques,
12, 6695–6719, https://doi.org/https://doi.org/10.5194/amt-12-6695-2019, publisher: Copernicus GmbH, 2019.

Lespinas, F., Wang, Y., Broquet, G., Bréon, F.-M., Buchwitz, M., Reuter, M., Meijer, Y., Loescher, A., Janssens-Maenhout, G., Zheng, B.,
and Ciais, P.: The potential of a constellation of low earth orbit satellite imagers to monitor worldwide fossil fuel CO2 emissions from
large cities and point sources, Carbon Balance and Management, 15, 18, https://doi.org/10.1186/s13021-020-00153-4, 2020.

Levin, I., Kromer, B., Schmidt, M., and Sartorius, H.: A novel approach for independent budgeting of fossil fuel CO2 over Europe by 14CO2
observations, Geophysical Research Letters, 30, https://doi.org/10.1029/2003GL018477, number: 23 Reporter: Geophysical Research
Letters, 2003.

López, R., Guillén, J., Fiore, G., M'Barek, R., Tamosiunas, S., Camia, A., Banja, M., Cazzaniga, N. E., Gurría, P., García Condado, S.,
Jonsson, R., and Ronzon, T.: Biomass flows in the European Union: the Sankey biomass diagram – towards a cross set integration of
biomass, Publications Office of the European Union, https://data.europa.eu/doi/10.2760/352412, 2017.

Mahadevan, P., Wofsy, S. C., Matross, D. M., Xiao, X., Dunn, A. L., Lin, J. C., Gerbig, C., Munger, J. W., Chow, V. Y., and Gottlieb, E. W.: A satellite-based biosphere parameterization for net ecosystem CO2 exchange: Vegetation Photosynthesis and Respiration Model (VPRM), Global Biogeochemical Cycles, 22, https://doi.org/10.1029/2006GB002735, number: 2 Reporter: Global Biogeochemical Cycles, 2008.

670 Marshall, J., Nuñez Ramirez, T., and partners, W. C.: Attribution Problem Configurations, Tech. rep., CO2 Human Emissions, H2020 European Project, https://www.che-project.eu/sites/default/files/2020-01/CHE-D4-3-V4-1.pdf, 2019.

Menut, L., Bessagnet, B., Khvorostyanov, D., Beekmann, M., Blond, N., Colette, A., Coll, I., Curci, G., Foret, G., Hodzic, A., Mailler, S., Meleux, F., Monge, J.-L., Pison, I., Siour, G., Turquety, S., Valari, M., Vautard, R., and Vivanco, M. G.: CHIMERE 2013: a model for regional atmospheric composition modelling, Geoscientific Model Development, 6, 981–1028, https://doi.org/10.5194/gmd-6-981-2013,

675 2013.

Naipal, V., Ciais, P., Wang, Y., Lauerwald, R., Guenet, B., and Van Oost, K.: Global soil organic carbon removal by water erosion under climate change and land use change during AD 1850–2005, Biogeosciences, 15, 4459–4480, https://doi.org/10.5194/bg-15-4459-2018, 2018.

Pillai, D., Buchwitz, M., Gerbig, C., Koch, T., Reuter, M., Bovensmann, H., Marshall, J., and Burrows, J. P.: Tracking city CO_2 emissions

680 from space using a high-resolution inverse modelling approach: a case study for Berlin, Germany, Atmospheric Chemistry and Physics, 16, 9591–9610, https://doi.org/10.5194/acp-16-9591-2016, 2016.

Pinty, B., Janssens-Maenhout, G., Dowell, M., Zunker, H., Brunhes, T., Ciais, P., Dee, D., Denier van der Gon, H. A. C., Dolman, H., Drinkwater, M., Engelen, R., Heimann, M., Holmlund, K., Husband, R., Kentarchos, A., Meyer, A., Palmer, P., and Scholze, M.: An operational anthropogenic CO2 emissions monitoring and verification support capacity. Baseline requirements, model components and

685 functional architecture, Tech. rep., European Commission Joint Research Centre, Ispara, Italy, https://doi.org/10.2760/08644, 2017.

Portmann, F. T., Siebert, S., and Döll, P.: MIRCA2000—Global monthly irrigated and rainfed crop areas around the year 2000: A new high-resolution data set for agricultural and hydrological modeling, Global Biogeochemical Cycles, 24, https://doi.org/https://doi.org/10.1029/2008GB003435, 2010.

Santaren, D., Broquet, G., Bréon, F.-M., Chevallier, F., Siméoni, D., Zheng, B., and Ciais, P.: A local- to national-scale inverse modeling sys-

690 tem to assess the potential of spaceborne CO_2 measurements for the monitoring of anthropogenic emissions, Atmospheric Measurement Techniques, 14, 403–433, https://doi.org/10.5194/amt-14-403-2021, 2021.

Schwandner, F. M., Gunson, M. R., Miller, C. E., Carn, S. A., Eldering, A., Krings, T., Verhulst, K. R., Schimel, D. S., Nguyen, H. M., Crisp, D., O'Dell, C. W., Osterman, G. B., Iraci, L. T., and Podolske, J. R.: Spaceborne detection of localized carbon dioxide sources, Science, 358, eaam5782, https://doi.org/10.1126/science.aam5782, 2017.

695 Staufer, J., Broquet, G., Bréon, F.-M., Puygrenier, V., Chevallier, F., Xueref-Rémy, I., Dieudonné, E., Lopez, M., Schmidt, M., Ramonet, M., Perrussel, O., Lac, C., Wu, L., and Ciais, P.: The first 1-year-long estimate of the Paris region fossil fuel CO2 emissions based on atmospheric inversion, Atmos. Chem. Phys., 16, 14 703–14 726, https://doi.org/10.5194/acp-16-14703-2016, number: 22 Reporter: Atmos. Chem. Phys., 2016.

Stuiver, M. and Polach, H. A.: Discussion Reporting of 14C Data, Radiocarbon, 19, 355–363, https://doi.org/10.1017/S0033822200003672,

700 number: 3 Reporter: Radiocarbon, 1977.

Super, I., Dellaert, S. N. C., Visschedijk, A. J. H., and Denier van der Gon, H. A. C.: Uncertainty analysis of a European high-resolution emission inventory of CO_2 and CO to support inverse modelling and network design, Atmospheric Chemistry and Physics, 20, 1795–1816, https://doi.org/https://doi.org/10.5194/acp-20-1795-2020, publisher: Copernicus GmbH, 2020.

Tarantola, A.: Inverse Problem Theory and Methods for Model Parameter Estimation, Society for Industrial and Applied Mathematics, https://doi.org/10.1137/1.9780898717921, 2005.

Turnbull, J., Rayner, P., Miller, J., Naegler, T., Ciais, P., and Cozic, A.: On the use of 14CO2 as a tracer for fossil fuel CO2: Quantifying uncertainties using an atmospheric transport model, Journal of Geophysical Research: Atmospheres, 114, https://doi.org/https://doi.org/10.1029/2009JD012308, 2009.

Wang, Y.: The potential of observations of radiocarbon in atmospheric CO2 for the atmospheric inversion of fossil fuel CO2 emission at regional scale, Ph.D. thesis, Université Paris Saclay, https://tel.archives-ouvertes.fr/tel-01529200, 2016.

Wang, Y., Broquet, G., Ciais, P., Chevallier, F., Vogel, F., Kadygrov, N., Wu, L., Yin, Y., Wang, R., and Tao, S.: Estimation of observation errors for large-scale atmospheric inversion of CO2 emissions from fossil fuel combustion, Tellus B: Chemical and Physical Meteorology, 69, 1325 723, https://doi.org/10.1080/16000889.2017.1325723, number: 1 Reporter: Tellus B: Chemical and Physical Meteorology, 2017.

Wang, Y., Broquet, G., Ciais, P., Chevallier, F., Vogel, F., Wu, L., Yin, Y., Wang, R., and Tao, S.: Potential of European 14CO2 observation network to estimate the fossil fuel CO2 emissions via atmospheric inversions, Atmos. Chem. Phys., 18, 4229–4250, https://doi.org/10.5194/acp-18-4229-2018, number: 6 Reporter: Atmos. Chem. Phys., 2018.

Wang, Y., Broquet, G., Bréon, F.-M., Lespinas, F., Buchwitz, M., Reuter, M., Meijer, Y., Loescher, A., Janssens-Maenhout, G., Zheng, B., and Ciais, P.: PMIF v1.0: assessing the potential of satellite observations to constrain CO_2 emissions from large cities and point sources over the globe using synthetic data, Geoscientific Model Development, 13, 5813–5831, https://doi.org/https://doi.org/10.5194/gmd-13-5813-2020, publisher: Copernicus GmbH, 2020.

Wu, L., Broquet, G., Ciais, P., Bellassen, V., Vogel, F., Chevallier, F., Xueref-Remy, I., and Wang, Y.: What would dense atmospheric observation networks bring to the quantification of city CO2 emissions?, Atmospheric Chemistry and Physics, 16, 7743–7771, https://doi.org/10.5194/acp-16-7743-2016, number: 12 Reporter: Atmospheric Chemistry and Physics, 2016.

Zazzeri, G., Yeomans, E. A., and Graven, H. D.: Global and regional emissions of radiocarbon from nuclear power plants from 1972 to 2016, Radiocarbon, pp. 1–15, https://doi.org/10.1017/RDC.2018.42, reporter: Radiocarbon, 2018.
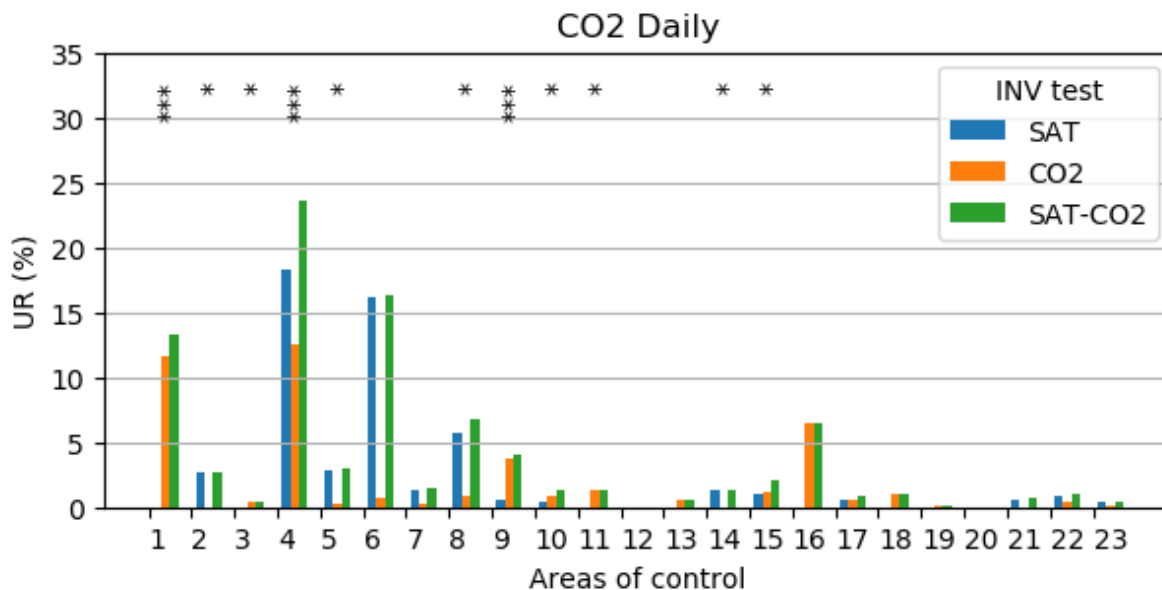
Figure A1. Uncertainty reduction in INV-SAT, INV-CO2 and INV-SAT-CO2 inversions for 24-h budgets of FF emissions of each controlled area in the main area of interest. The number of stars indicates the number of stations in each controlled area. The areas are listed in Table 1.
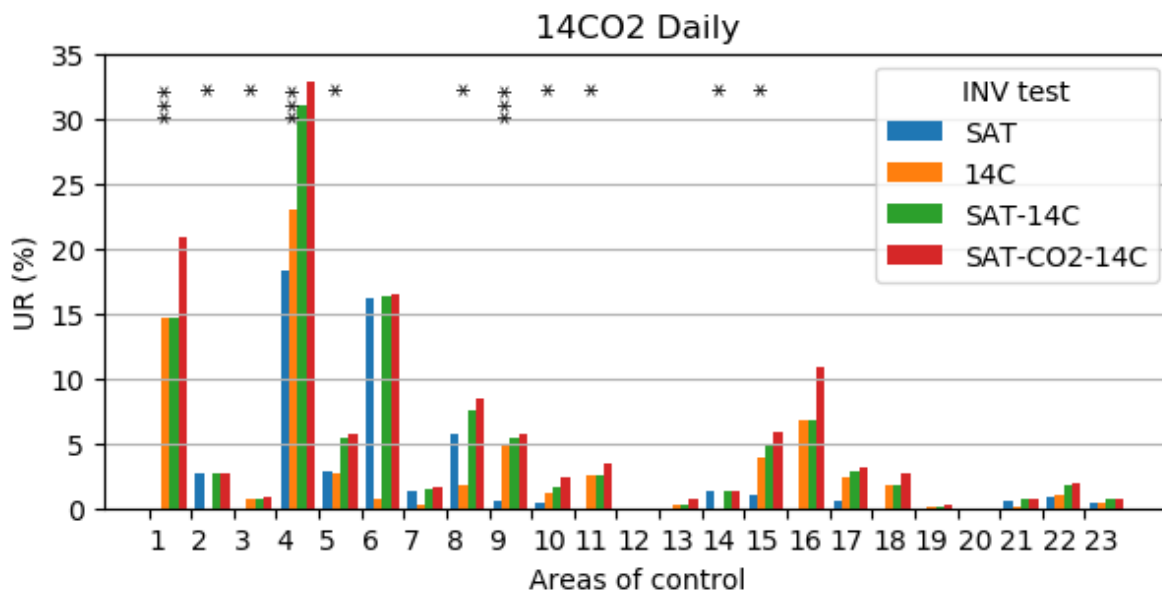
Figure A2. Uncertainty reduction in INV-SAT, INV-14C, INV-SAT-14C and INV-SAT-CO2-14C inversions for 24-h budgets of FF emissions of each controlled area in the main area of interest. The number of stars indicate the number of stations in each controlled area. The areas are listed in Table 1.
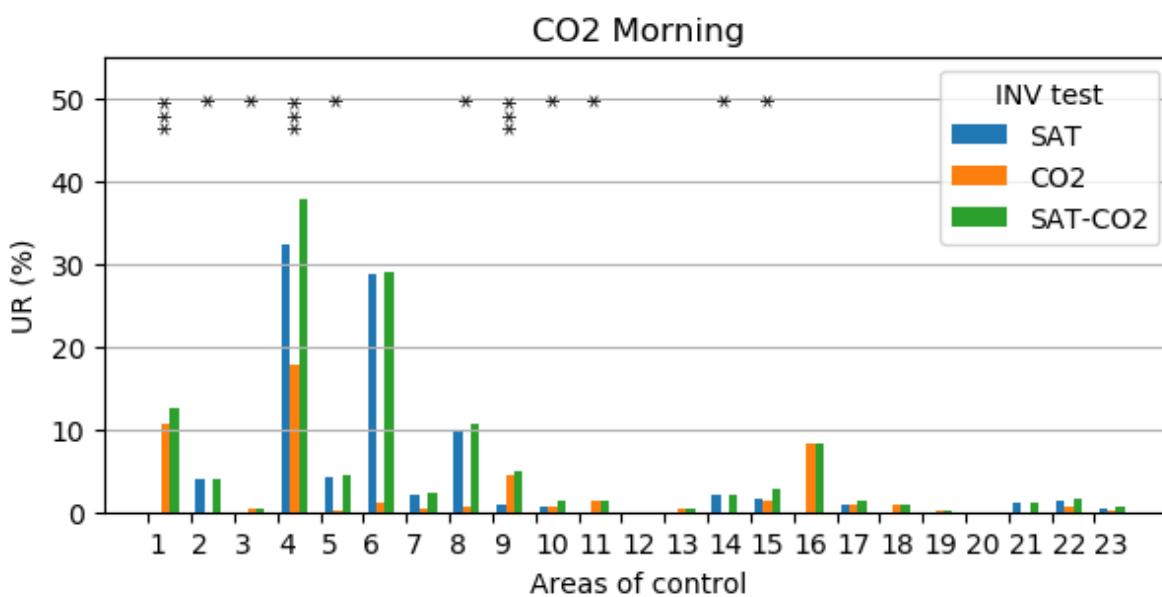
Figure A3. Uncertainty reduction in INV-SAT, INV-CO2, INV-SAT-CO2 inversions for morning budgets of FF emissions of each controlled area in the main area of interest. The number of stars indicates the number of stations in each controlled area. The controlled areas are listed in Table 1.
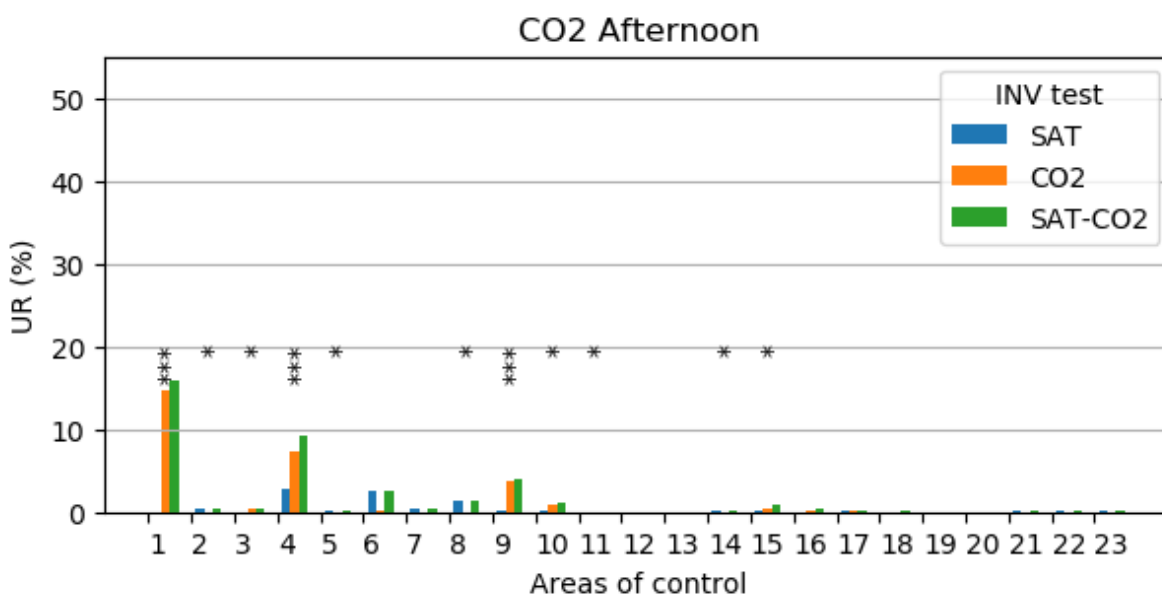
Figure A4. Uncertainty reduction in INV-SAT, INV-CO2, INV-SAT-CO2 inversions for afternoon budgets of FF emissions of each controlled area in the main area of interest. The number of stars indicates the number of stations in each controlled area. The names of the controlled areas are listed in Table 1.
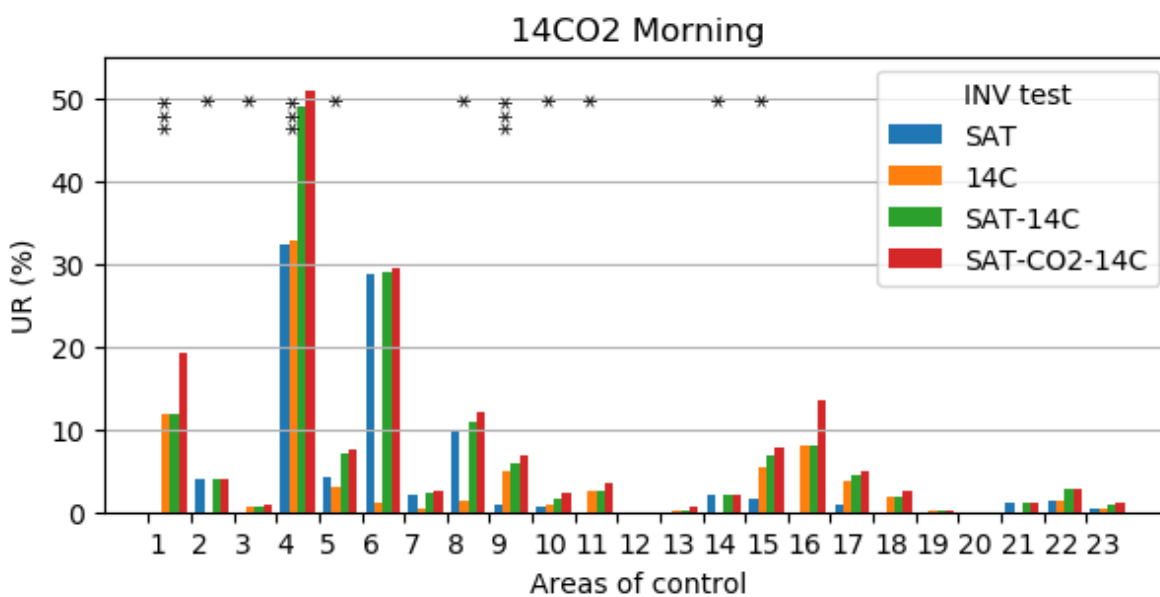
Figure A5. Uncertainty reduction in INV-SAT, INV-14C, INV-SAT-14C and INV-SAT-CO2-14C inversions for morning budgets of FF emissions of each controlled area in the main area of interest. The number of stars indicates the number of stations in each controlled area. The names of the controlled areas are listed in Table 1.
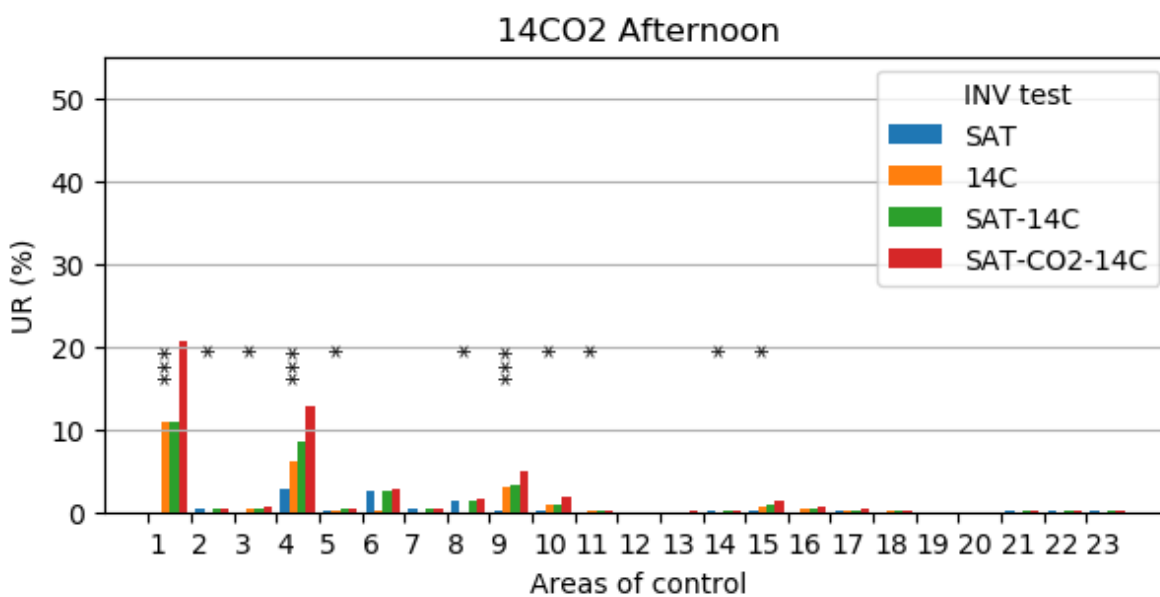
Figure A6. Uncertainty reduction in INV-SAT, INV-14C, INV-SAT-14C and INV-SAT-CO2-14C inversions for afternoon budgets of FF emissions of each controlled area in the main area of interest. The number of stars indicates the number of stations in each controlled area. The names of the controlled areas are listed in Table 1.
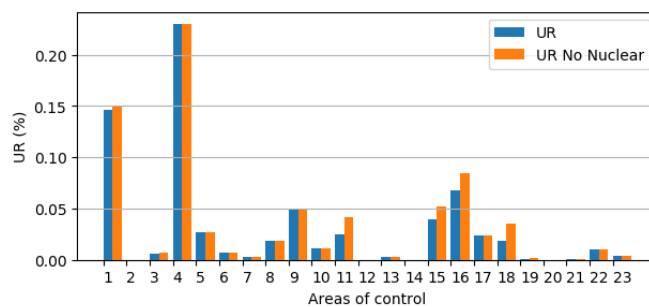
(a) UR on FF
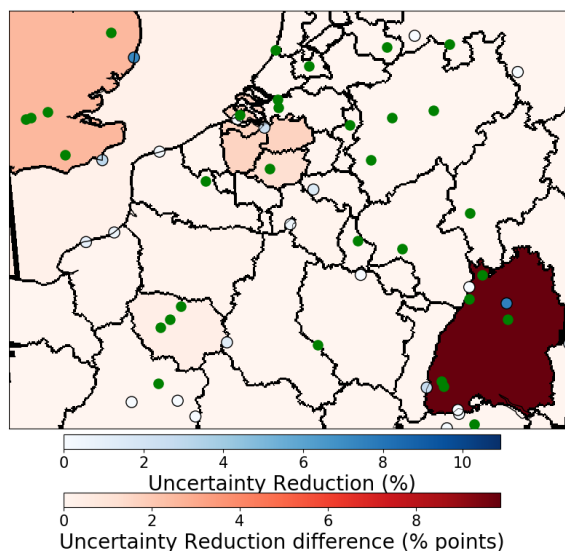
(b) ΔUR on FF budgets and UR on F^{14C} nuclear power plant budgets

Figure A7. (a) Uncertainty reductions, on 24-h FF budgets, with and without nuclear emissions in INV-14C inversion, for each controlled area in the main area of interest. The names of the controlled areas are listed in Table 1. (b) Maps, on the 2-km-resolution area, of the differences between uncertainty reductions with and without nuclear emissions (red palette) in INV-14C inversions and uncertainty reductions on F^{14C} nuclear power plant budgets (dots, blue palette). Green dots indicate the ground stations.